

Analysis of the weak lensing mass-richness relation of redMaPPer clusters in the LSST DESC DC2 simulations

Constantin Payerne,^{1,2,*} Zhuowen Zhang,³ Michel Aguena,^{4,5} Céline Combet,² Thibault Guillemin,⁶ Marina Ricci,⁴ Nathan Amouroux,⁶ Camille Avestruz,^{7,8} Eduardo J. Barroso,⁶ Arya Farahi,^{9,10} Eve Kovacs,¹¹ Calum Murray,^{4,12} Markus M. Rau,^{13,14} Eli S. Rykoff,^{15,16} Samuel J. Schmidt,¹⁷ and the LSST Dark Energy Science Collaboration

¹ Université Paris-Saclay, CEA, IRFU, 91191, Gif-sur-Yvette, France

² Université Grenoble Alpes, CNRS, IN2P3, LPSC, 38000 Grenoble, France

³ Kavli Institute for Cosmological Physics, University of Chicago, Chicago, IL 60637, USA

⁴ Université Paris Cité, CNRS, IN2P3, APC, 75013 Paris, France

⁵ Italian National Institute of AstroPhysics, Osservatorio Astronomico di Trieste, Italy

⁶ Université de Savoie, CNRS, IN2P3, LAPP, Annecy-le-Vieux, France

⁷ Department of Physics, University of Michigan, Ann Arbor, MI 48109, USA

⁸ Leinweber Center of Theoretical Physics, University of Michigan, Ann Arbor, MI 48109, USA

⁹ Department of Statistics and Data Sciences, The University of Texas at Austin, TX 78712, USA

¹⁰ The NSF-Simons AI Institute for Cosmic Origins, University of Texas at Austin, Austin, TX 78712, USA

¹¹ HEP Division, Argonne National Laboratory, 9700 S. Cass Ave., Lemont, IL 60439, USA

¹² Université Paris-Saclay, Université Paris Cité, CEA, CNRS, AIM, 91191, Gif-sur-Yvette, France

¹³ School of Mathematics, Statistics and Physics, Newcastle University, Newcastle upon Tyne, NE17RU, United Kingdom

¹⁴ High Energy Physics Division, Argonne National Laboratory, Lemont, IL 60439, USA

¹⁵ Kavli Institute for Particle Astrophysics & Cosmology, P. O. Box 2450, Stanford University, Stanford, CA 94305, USA

¹⁶ SLAC National Accelerator Laboratory, Menlo Park, CA 94025, USA

¹⁷ Department of Physics and Astronomy, University of California, One Shields Avenue, Davis, CA 95616, USA

February 13, 2025

ABSTRACT

Context. Cluster scaling relations are key ingredients in cluster abundance-based cosmological studies. In optical cluster cosmology, where clusters are detected through their richness, cluster-weak gravitational lensing has proven to be a powerful tool to constrain the cluster mass-richness relation. This work is conducted as part of the Dark Energy Science Collaboration (DESC), which aims to analyze the Legacy Survey of Space and Time (LSST) of Vera C. Rubin Observatory, starting in 2026.

Aims. Weak lensing-inferred cluster properties, such as mass, suffer from several sources of bias. In this paper, we aim to test the impact of modeling choices and observational systematics in cluster lensing on the inference of the mass-richness relation.

Methods. We constrain the mass-richness relation of 3,600 clusters detected by the redMaPPer algorithm in the cosmoDC2 extragalactic mock catalog (covering 440 deg²) of the LSST DESC DC2 simulation, using number count measurements and stacked weak lensing profiles in several intervals of richness ($20 \leq \lambda \leq 200$) and redshift ($0.2 \leq z \leq 1$).

Results. By modeling the mean of the scaling relation as $\langle \ln \lambda | M_{200c}, z \rangle = \ln \lambda_0 + \mu_z \log[(1+z)/(1+0.5)] + \mu_m [\log_{10}(M_{200c}) - 14.3]$, our baseline constraints are $\ln \lambda_0 = 3.37 \pm 0.03$, $\mu_z = 0.08 \pm 0.07$ and $\mu_m = 2.18 \pm 0.07$. We have found that, for a LSST-like source galaxy density, our constraints are robust to a change in concentration-mass relation and dark matter density profile modeling choices, when source redshifts and shapes are perfectly known. We have found that photometric redshift uncertainties can introduce bias at the 1σ level, which can be mitigated by an overall correcting factor, fitted jointly with scaling parameters. We find that including positive shear-richness covariance in the fit shifts the results by up to 0.5σ . We also found that our constraints fairly compare to a fiducial mass-richness relation, obtained from matching cosmoDC2 halos masses to redMaPPer-detected cluster richnesses.

Key words. Galaxies: clusters: general - Gravitational lensing: weak –methods: statistical

1. Introduction

Galaxy clusters have been essential in the construction of the standard model of cosmology, providing some of the first evidence of dark matter (Zwicky 1937) through the motions of galaxies within galaxy clusters and their spatial distribution provided evidence for the primordial origin of density fluctuations (Kaiser 1984). They originate from the gravitational collapse of large matter overdensities, that decouple from the expansion and form galaxy clusters. They represent the most massive structures

in the Universe held by gravity. Their formation history and their spatial and mass distributions are strongly dependent on the nature of gravity, the growth rate of large-scale structures, and the Universe's expansion history (Bartlett 1997; Allen et al. 2011; Kravtsov & Borgani 2012).

The abundance of clusters has been a widely used cosmological probe for the last 20 years, e.g., using X-ray clusters detected by the ROSAT All-Sky Survey (Mantz et al. 2015), XMM-Newton (Pacaud et al. 2018) or eROSITA (Ghirardini et al. 2024), clusters detected through their Sunyaev-Zeldovich effect by the *Planck* satellite (Ade et al. 2014, 2016), the South Pole

* Corresponding author: e-mail: constantin.payerne@gmail.com

Telescope (SPT, Bocquet et al. (2024); Vogt et al. (2024)) or the Atacama Cosmology Telescope (ACT, Hasselfield et al. (2013)), but also using clusters detected through the galaxy member population such as by the Dark Energy Survey (DES, Abbott et al. (2020)), the Kilo degree Survey (KiDS, Lesci et al. (2022)), SDSS (Fumagalli et al. 2023) or with shear-selected clusters with HSC (Chiu et al. 2024) (see Table 2 in Payerne et al. (2024) that recaps the cluster abundance-based cosmological analyses before June 2024). Over the years, cluster abundance has proven to provide competitive and complementary constraints with other large-scale structure probes, geometrical probes, and with the analysis of the Cosmic Microwave Background, especially on the total amount of matter in the Universe and the amplitude of matter fluctuations.

The constraining power of cluster number counts is currently limited by our understanding of the cluster scaling relations (Pratt et al. 2019; Costanzi et al. 2019; Abbott et al. 2020), i.e., the statistical relationship between the cluster observables and their total masses. At optical wavelengths, clusters are often detected through the color and brightness of their member galaxies (Rykoff et al. 2014), but clusters of galaxies can also be identified as high signal-to-noise ratio peaks detected on the weak-lensing aperture mass maps (Hettterscheidt et al. 2005; Chen et al. 2024).

At optical wavelength, weak gravitational lensing has become a robust tool to constrain cluster masses (McClintock et al. 2019; Umetsu 2020; Murray et al. 2022; Mistele & Durakovic 2024; Grandis et al. 2024), through the coherent distortion in the shapes of background galaxies, due to the bending of the light path by the cluster gravitational field. Cluster abundance and cluster weak lensing information (using either masses or profiles directly) are usually combined, since they display different degeneracies on scaling relation parameters and cosmology, enabling tightening constraints of both cosmological parameters and cluster scaling relations (Mantz et al. 2015; Murata et al. 2019; Mulroy et al. 2019; Abbott et al. 2020; Lesci et al. 2022; Sunayama et al. 2023). However, the mapping between the measurement of weak gravitational lensing and cluster masses is not well understood, as it is impacted by several sources of statistical noises and systematic uncertainties (Köhlinger et al. 2015; Grandis et al. 2021).

First, weak lensing cluster mass reconstruction is statistically limited by the number density of galaxies or depth. Ongoing surveys such as DES, KiDS, HSC or the *Euclid* mission (Laureijs et al. 2011) and future wide optical surveys such as the Legacy Survey of Space and Time¹ (LSST, Abell et al. (2009)) or the Nancy Grace Roman Space Telescope (Spergel et al. 2015) provide or will provide a large influx of data to reduce statistical uncertainties in lensing measurement at an unprecedented level. Other statistical noises affect the measurement of the cluster lensing signal, such as the intrinsic variability of cluster morphology, line-of-sight correlated structures, galaxy shape intrinsic variation, or even the size of the cluster catalog in stacking strategies.

Second, several systematic biases may affect the cluster mass inference. Some are related to "theoretical uncertainties", such as unknowns in the modeling of the dark matter density in cluster field (Becker & Kravtsov 2011; Lee et al. 2018), the modeling of the presence of baryons (Cromer et al. 2022). Other biases are more directly related to the observations themselves and may arise from the shear calibration (Hernández-Martín et al. 2020), the calibration of the photometric redshift distribution of the background galaxy sample (Wright et al. 2020), the contamina-

tion of the source galaxy sample by foreground galaxies (Varga et al. 2019), miscentering (mis-identification of the cluster center Sommer et al. (2022)), or from selection effects² of cluster finding algorithms. All of these sources of scatter and bias have to be carefully controlled, in light of the unprecedented volume and quality of lensing data provided by the upcoming large-footprint lensing surveys.

The Vera Rubin Observatory in Chile will conduct the Legacy Survey of Space and Time, a 10-year wide-field imaging survey that will cover 18,000 deg² of the southern sky starting by the end of 2025 (Abell et al. 2009). The LSST aims to measure the shapes and redshifts of a few billion galaxies up to $z \sim 3$, which will allow to measure number counts and weak gravitational lensing of $\sim 100,000$ galaxy clusters up to $z \sim 1$ (Abell et al. 2009). In this context, the LSST Dark Energy Science Collaboration (2012)³ is preparing the cosmological analysis of the upcoming LSST data.

In this work, we make use of the LSST DESC Data Challenge 2 (DC2, Korytov et al. (2019); Abolfathi et al. (2021)) simulated dataset. We aim to infer the mass-richness relation of redMaPPer-detected galaxy clusters in DC2, from a combination of cluster weak lensing and abundance. All fits will be performed at fixed cosmology, chosen to be the fiducial cosmology of the DC2 simulation, which is close to the seven-year *Wilkinson Microwave Anisotropy Probe* best-fit Λ CDM values (WMAP, Komatsu et al. (2011)) given by $\omega_{\text{cdm}} = 0.1109$, $\omega_{\text{b}} = 0.02258$, $n_{\text{s}} = 0.963$, $h = 0.71$, $\sigma_8 = 0.8$, and $w = -1$. We investigate the robustness of the inferred scaling parameters to a change in several modeling choices widely used in the literature (dark matter density profile, concentration-mass relation), as well as in the presence of observational systematics. This work allows us to showcase the use of some of the software tools developed in the DESC in concrete cluster analysis, and provide some conclusions on the precision and accuracy of the inferred mass-richness relation with DC2 statistics, in the light of the LSST data.

The paper is organized as follows; In Section 2, we present the modeling of the scaling relation that we use in this paper, as well as the formalism for cluster abundance and cluster lensing cosmology. In Section 3 we review the different inference methods to constrain the scaling relation from cluster lensing and abundance. We present in Section 4 the DC2 dataset, and construct in Section 5 the cluster count and weak lensing data vectors that we consider. Finally, we present in Section 6 the constraints on the DC2 cluster scaling relation, and explore different systematic effects that impact cluster lensing analyses, before concluding in Section 7.

2. Formalism used in this paper

2.1. Cluster mass-richness relation

This paper aims to infer the cluster scaling relation using a combination of cluster lensing profiles and abundance. Due to the stochastic process of cluster formation and baryon physics occurring in its innermost regions, the cluster richness λ is a statistical variable for a halo with fixed mass m . In this paper, we consider the log-normal scaling relation $P(\lambda|m, z)$ given by (see e.g. Mantz et al. 2008; Evrard et al. 2014; Saro et al. 2015; Farahi

² These can be due to e.g., projection effects (Wu et al. 2022) or physically unassociated galaxies counted as cluster member galaxies (Lee et al. 2024).

³ <http://lsstdesc.org>

¹ <http://www.lsst.org>

et al. 2018; Murata et al. 2019; Anbajagane et al. 2020)

$$P(\ln \lambda|m, z) = \frac{1}{\sqrt{2\pi}\sigma_{\ln \lambda|m, z}} \exp \left\{ -\frac{[\ln \lambda - \langle \ln \lambda|m, z \rangle]^2}{2\sigma_{\ln \lambda|m, z}^2} \right\}, \quad (1)$$

where

$$\langle \ln \lambda|m, z \rangle = \ln \lambda_0 + \mu_z \ln \left(\frac{1+z}{1+z_0} \right) + \mu_m \log_{10} \left(\frac{m}{m_0} \right), \quad (2)$$

and

$$\sigma_{\ln \lambda|m, z} = \sigma_{\ln \lambda_0} + \sigma_z \ln \left(\frac{1+z}{1+z_0} \right) + \sigma_m \log_{10} \left(\frac{m}{m_0} \right). \quad (3)$$

In the above equation, $\sigma_{\ln \lambda|m, z}$ is the total error, i.e. including contributions of the richness measurement errors and the intrinsic scatters (see e.g. Murata et al. (2019)). It is possible to split the two contributions by adding a Poisson variance term (Zhang et al. 2023) in Eq. (3) (see Appendix B). Let us note that the *forward* modeling $P(\lambda|m, z)$ is different from the *backward* formalism $P(m|\lambda, z)$, which was used in several other works (see e.g. Baxter et al. 2016; Melchior et al. 2017; Simet et al. 2017; Jimeno et al. 2018; McClintock et al. 2019). In this work, we consider the pivot redshift $z_0 = 0.5$ and pivot mass $m_0 = 10^{14.3} M_\odot$. From the above, the cluster scaling relation has 6 free parameters; $\ln \lambda_0$, μ_z , and μ_m denote respectively the offset richness, the redshift dependence, and mass dependence of the mean cluster scaling relation, where the offset variance of the relation is given by $\sigma_{\ln \lambda_0}$, and σ_z and σ_m denote the redshift and mass dependency of the variance.

2.2. Cluster number count

2.2.1. Measuring cluster number counts

In combination with cluster weak lensing information, we will use cluster number counts to investigate the mass-richness relation of galaxy clusters. As we will consider *stacked* (averaged) cluster lensing profiles, we consider the binned approach for counts by consistency (Abbott et al. 2020; Lesci et al. 2022; Fumagalli et al. 2023), i.e. counting clusters in 4×7 richness-redshift intervals (see Section 5). Let us note that the binned approach is not the unique method, since the unbinned approach (Penna-Lima et al. 2014; Payerne et al. 2024) is also often used in the literature (see e.g. Mantz et al. (2015); Bocquet et al. (2023); Ghirardini et al. (2024)), and considers an infinite number of richness-redshift bins, such as the count is at most equal to one.

2.2.2. Modeling cluster number counts

For richness-detected clusters, the redshift-richness cluster number density is given by

$$\frac{d^2 N(\lambda, z)}{d\Omega dz d\lambda} = \int_{m_{\min}}^{m_{\max}} dm \frac{dn(m, z)}{dm} \frac{d^2 V(z)}{dz d\Omega} \Phi(\lambda, m, z) P(\lambda|m, z), \quad (4)$$

where Ω is the survey sky area⁴, $P(\lambda|m, z)$ corresponds to the forward modeling of the mass-richness relation as presented above, $dn(m, z)/dm$ is the halo mass function (predicting the comoving number density of dark matter halos per mass interval), $d^2 V(z)/dz d\Omega$ is the differential comoving volume, and $\Phi(\lambda, m, z)$

is the cluster selection function. The partial comoving volume is given by

$$\frac{d^2 V(z)}{dz d\Omega} = d_H \frac{D_C^2(z)}{H(z)/H_0} \quad (5)$$

where $H(z)$ is the Hubble parameter at redshift z (the Hubble constant is given by $H_0 = H(z=0)$), $d_H = c/H_0$ is the Hubble distance, and D_C is the radial comoving distance (Hogg 1999). The masses m_{\min} and m_{\max} correspond to the minimum and maximum mass accessible in the survey, generally set by the survey strategy or the selection function. Throughout this paper, we set $m_{\min} = 10^{12} M_\odot$ and $m_{\max} = 10^{15.5} M_\odot$ for the minimum and maximum halo masses to evaluate the halo mass integration in the model predictions for the cluster observables.

The selection function Φ denotes our ability to detect clusters. It is associated with the cluster finder algorithm performances and survey strategy, and its calibration plays a crucial role in cluster-based cosmological analyses. The selection function of a cluster finder can be assessed by (i) using end-to-end simulated data, geometrically matching the observed cluster catalog to the underlying dark matter halo population (Euclid Collaboration et al. 2019; Lesci et al. 2022; Bulbul et al. 2024), (ii) injecting mock clusters in the real dataset (Rykoff et al. 2014; Rykoff et al. 2016; Planck Collaboration et al. 2016), or by (iii) cross-validating the cluster finder performances using comparison between datasets at different wavelengths (Sadibekova et al. 2014; Saro et al. 2015). It is generally separated in two components, $\Phi = c(m, z)/p(\lambda_{\text{obs}}, z_{\text{obs}})$ (see e.g. Aguena & Lima 2018). First, the *completeness* $c(m, z)$ gives the fraction of true underlying dark matter halos the cluster finder algorithm detects. If the completeness is less than 1, then an underlying dark matter halo population is systematically missing from our dataset (Mantz 2019). Second, the *purity* $p(\lambda_{\text{obs}}, z_{\text{obs}})$ denotes the fraction of "spurious" detections in the cluster catalog (false positives, mis-identified structures along the line-of-sight), where λ_{obs} and z_{obs} are the *observed* richness and redshift. We refer the reader to Section 4.3, in which we use the first method to assess the selection function (purity and completeness) of the redMaPPer cluster in the DC2 simulations. In the following, we consider that the richness $\lambda = \lambda_{\text{obs}}$, such as the mass-richness relation in Eq. (1) accounts for the total dispersion of richness measurement (intrinsic and observed), as stated before.

With all these elements, the predicted cluster number count N_{ij} in the i -th richness and j -th redshift bin is finally given by

$$N_{ij} = \Omega \int_{z_i}^{z_{i+1}} dz \int_{\lambda_j}^{\lambda_{j+1}} d\lambda \frac{d^2 N(\lambda, z)}{d\Omega dz d\lambda}. \quad (6)$$

2.2.3. Cluster count covariance

The cluster count covariance accounts for two principal contributions: the Poisson shot noise and the Super-Sample Covariance (SSC). First, the Poisson noise affects the counting of clusters in uncorrelated bins (Poisson 1837). Second, the SSC denotes the contribution from the intrinsic fluctuations of the matter overdensity field, within and beyond the survey volume (Hu & Kravtsov 2003). As a result, SSC introduces a covariance between the counts in different bins and increases their variance. SSC is of particular importance in cluster abundance-based likelihoods since it impacts the precision of the recovered cosmological parameters by $\sim 20\%$ for surveys like the Vera C. Rubin LSST or the *Euclid* mission (Fumagalli et al. 2021; Payerne et al. 2023; Payerne et al. 2024), which will detect $\sim 100,000$

⁴ Here, we consider the survey depth is uniform across the sky.

clusters. The shot-noise and SSC contributions can be estimated via resampling techniques directly on the data such as jackknife resampling (Escoffier et al. 2016). However, since the sample of clusters detected on the DC2 galaxy catalog is relatively small, the noise in the jackknife estimation of the cluster count matrix is important. We rather choose to use the covariance prediction

$$\Sigma_{\text{N}}[ij, kl] = N_{ij}\delta_{ik}^K\delta_{jl}^K + N_{ij}N_{kl}\langle b \rangle_{ij}\langle b \rangle_{kl}S_{jl}. \quad (7)$$

In the above equation, the first term denotes the Poisson shot noise, (scaling with the count N_{ij}), where δ_{ik}^K is the Kronecker delta function. The second term denotes the SSC term, where $\langle b \rangle_{ik}$ is the average halo bias in the ik -th redshift-richness bin, N_{ij} is the predicted cluster count in Eq. (6), and $S_{jl} = \langle \delta_{m,j}\delta_{m,l} \rangle$ is the covariance between the smoothed matter overdensities respectively in the j -th and l -th redshift bin (Lacasa et al. 2018). Let us note that, opposite to Poisson noise, the SSC variance scales with N_{ij}^2 .

2.3. Cluster weak gravitational lensing

The observed ellipticity ϵ^{obs} of a lensed source galaxy is related to its intrinsic (un-lensed) shape ϵ^{int} given by (Schneider et al. 1992)

$$\epsilon^{\text{obs}} = \frac{\epsilon^{\text{int}} + g}{1 + g^*\epsilon^{\text{int}}}, \quad (8)$$

where $g = \gamma/(1 - \kappa)$ is the reduced shear, γ is the shear and κ is the convergence. In the weak lensing regime, we consider that $\kappa \ll 1$ at large scales, so the first order Taylor expansion in γ of the observed ellipticity gives $\epsilon^{\text{obs}} \approx \gamma + \epsilon^{\text{int}}$. Taking the average of the above expression and assuming that $\langle \epsilon^{\text{int}} \rangle = 0$ in the absence of large-scale galaxy intrinsic alignment, we get that the cluster local shear can be estimated statistically through $\langle \epsilon^{\text{obs}} \rangle \approx \gamma$. In practice, we decompose galaxy shapes in tangential and cross components, defined respectively by

$$\epsilon_+ + i\epsilon_\times = -\epsilon^{\text{obs}} \exp(-i2\phi) \quad (9)$$

where ϵ^{obs} is the observed ellipticity and ϕ is the polar angle of the source galaxy relative to the cluster center. From that, we get that $\langle \epsilon_+ \rangle = \gamma_+$, γ_+ is the *tangential* shear, and $\langle \epsilon_\times \rangle = \gamma_\times = 0$ for any mass distribution. Here, $\langle \cdot \rangle$ denotes the average along a closed (circular) loop (Bernstein & Nakajima 2009; Umetsu 2020).

2.3.1. Measuring the cluster excess surface density profile and covariance

The excess surface density $\Delta\Sigma(R)$ is commonly used as the cluster weak-lensing shear estimator (Mandelbaum et al. 2005; Murata et al. 2019; McClintock et al. 2019).

In this paper we explore cluster lensing through a stacking strategy, i.e. we estimate the excess surface density signal around an ensemble of clusters rather than for individual clusters. Stacked lensing allows us to increase the signal-to-noise ratio and is particularly interesting for low-mass clusters, for which the strength of gravitational lensing is weak. Moreover, the stacking strategy averages over the intrinsic triaxiality of individual halos and substructures (Corless & King 2009), thus recovering an effective sphericity, since stacked data are usually fitted using a spherical model. The maximum likelihood estimator of $\Delta\Sigma$ considering a stack of N_l clusters where each one has

N_{ls} background sources in the radial bin $[R, R + \Delta R]$ can be written (Shirasaki & Takada 2018; Sheldon et al. 2004)

$$\widehat{\Delta\Sigma}_+(R) = \frac{1}{\sum_{l=1}^{N_l} \sum_{s=1}^{N_{ls}} w_{ls}} \sum_{l=1}^{N_l} \sum_{s=1}^{N_{ls}} w_{ls} \widehat{\Sigma}_{\text{crit}}(z_s, z_l) \epsilon_+^{l,s}, \quad (10)$$

where the sum runs over all lens-source (l, s) pairs, located within the physical projected radius interval $[R, R + \Delta R]$ from the lens l . Here, $\epsilon_+^{l,s}$ is the tangential ellipticity of the galaxy s relative to the lens l . The quantity $\widehat{\Sigma}_{\text{crit}}(z_s, z_l)$ is the effective critical surface mass density of the lens-source system, averaged over the photometric (photo- z) redshift probability density function $p(z_s)$ of the galaxy with index s , such as

$$\widehat{\Sigma}_{\text{crit}}(z_s, z_l)^{-1} = \int_{z_l}^{+\infty} dz_s p(z_s) \Sigma_{\text{crit}}(z_s, z_l)^{-1}. \quad (11)$$

The critical surface mass density $\Sigma_{\text{crit}}(z_s, z_l)$ is a geometrical factor given by

$$\Sigma_{\text{crit}}(z_s, z_l) = \frac{c^2}{4\pi G} \frac{D_A(z_s)}{D_A(z_l)D_A(z_s, z_l)}, \quad (12)$$

where $D_A(z_l)$, $D_A(z_s)$ and $D_A(z_l, z_s)$ are respectively the physical angular diameter distance to the lens, to the source, and between the lens and the source (Hogg 1999). The weights w_{ls} maximize the signal-to-noise ratio for this estimator (Sheldon et al. 2004) and can be written as the product $w_{ls} = w_{ls}^{\text{geo}} w_{ls}^{\text{shape}}$ such as

$$w_{ls}^{\text{geo}} = \langle \widehat{\Sigma}_{\text{crit}}(z_s, z_l) \rangle^{-2}, \quad (13)$$

$$w_{ls}^{\text{shape}} = \frac{1}{\sigma_{\text{rms}}^2(\epsilon_s^+) + \sigma_{\text{meas}}^2(\epsilon_s^+)}. \quad (14)$$

The quantity $\sigma_{\text{rms}}(\epsilon_s^+)$ is the standard deviation of the tangential component of the ellipticity, whereas $\sigma_{\text{meas}}(\epsilon_s^+)$ denotes the error on shape measurement. In the ideal case where galaxy redshifts and shapes are perfectly known, these weights reduce to $w_{ls}^{\text{geo}} = \Sigma_{\text{crit}}^{-2}(z_s, z_l)$ and $w_{ls}^{\text{shape}} = \sigma_{\text{rms}}^{-2}(\epsilon_s^+)$.

Inferring scaling relation parameters requires knowing the covariance of the lensing profiles. The covariance originates from a variety of phenomena (see a recap in Hoekstra (2003); Wu et al. (2019); Gruen et al. (2015); McClintock et al. (2019)). The first major contribution is the intrinsic scatter in the shape of background galaxies combined with the limited sample of clusters and background galaxies. This contribution can be significantly decreased by increasing cluster/galaxy sample sizes. Second, the covariance accounts for the scattering induced by uncorrelated large-scale structures along the line of sight. Moreover, correlated structures around a cluster introduce an additive covariance in the measured lensing signal, associated with the variation of the two-halo term. Intrinsic fluctuations in halo properties within the stack (i.e. the variation of concentration at fixed mass, the halo ellipticity, and orientation) are an important source of scatter at lower scales. It may also denote the scatter in individual masses of richness-selected clusters within the stack.

As for cluster count, the cluster lensing profile covariance can be predicted analytically (see e.g. Wu et al. (2019)⁵) or using semi-analytical methods (see e.g. McClintock et al. (2019)).

⁵ Wu et al. (2019) has created the `cluster-lensing-cov`⁶ package, to provide analytical predictions of the excess surface density profile covariance.

Such approaches require modeling a large variety of data properties, such as the source sample/lens sample redshift distribution, dispersion of intrinsic shape, the dark matter halo density profile, the level of scatter in concentration/miscentering/morphology of the clusters in the redMaPPer catalog, etc. Here, we choose to rely on a simpler data-based method, which can estimate all these contributions at once with no underlying assumptions, and with relatively low computational costs. We implement bootstrap resampling (see e.g., [Simet et al. 2017](#); [Parroni et al. 2017](#)) as follows; for each stack, we create $N_{\text{boot}} = 400$ ensembles of clusters by selecting the same number of clusters but taking them with replacement. We compute N_{boot} times the stacked $\overline{\Delta\Sigma}$ profile for each bootstrap resampling, we compute the covariance matrix

$$[\Sigma_{\text{WLp}}]_{ij} = \frac{1}{N_{\text{boot}} - 1} \sum_{k=1}^{N_{\text{boot}}} [\Delta\Sigma^k(R_i) - \overline{\Delta\Sigma}(R_i)][\Delta\Sigma^k(R_j) - \overline{\Delta\Sigma}(R_j)], \quad (15)$$

where

$$\overline{\Delta\Sigma}(R_i) = \frac{1}{N_{\text{boot}}} \sum_{k=1}^{N_{\text{boot}}} \Delta\Sigma^k(R_i). \quad (16)$$

We keep only the diagonal terms since the off-diagonal terms are too noisy due to the low count statistics measured in each richness-redshift bin within the DC2 footprint. [Wu et al. \(2019\)](#) noted that neglecting off-diagonal terms at larger scales $R \geq 5 - 6$ Mpc will lead to an underestimation of the parameter errors inferred from weak lensing profiles (cluster mass, concentration, etc.) when shape noise (i.e. uncorrelated source of noise) is subdominant. In this work, we focus on the $R < 3.5$ Mpc region only, which will minimize this impact (see Section 6).

2.3.2. Modeling of the cluster excess surface density profile and stacked weak lensing mass

To model the stacked lensing signal, $\Delta\Sigma(R)$ can be related to the surface mass density of the cluster $\Sigma(R)$. For a perfectly centered cluster, it is given by

$$\Sigma(R) = \int_{-\infty}^{+\infty} dy \rho \left(\sqrt{y^2 + R^2} \right). \quad (17)$$

where ρ is the three-dimensional dark matter density. Then, $\Delta\Sigma$ is given by

$$\Delta\Sigma(R) = \Sigma(< R) - \Sigma(R). \quad (18)$$

where

$$\Sigma(< R) = \frac{2}{R^2} \int_0^R dR' R' \Sigma(R'). \quad (19)$$

The total matter content around clusters is parametrized by the three-dimensional density $\rho(r)$ (and by extension $\Sigma(R)$ through Eq. (17)).

There are two contributions to the matter density. First, the matter density originates from the cluster itself, called the 1-halo term, generally assuming to follow fitting function calibrated on simulation such as the Navarro-Frank-White (NFW, [Navarro et al. \(1997\)](#)) profile, when assuming sphericity. It is common to parameterize the one-halo excess surface density $\Delta\Sigma_{1h}$ using the spherical overdensity mass M_{200c} given by

$$M_{200c} = \frac{4\pi r_{200c}^3}{3} 200\rho_c(z) \quad (20)$$

where r_{200c} is the radius of the sphere that contains an average matter density 200 times higher than the critical density $\rho_c(z)$. Such profiles also depend on an additive concentration parameter c_{200c} , quantifying the level of concentration of mass in the innermost regions of the cluster. Second, the matter density around clusters also originates from their surrounding halos. From [Oguri & Takada \(2011\)](#), the two-halo excess surface density is given by

$$\Delta\Sigma_{2h}(R) = \frac{\rho_m(z) b_h(M_{200c}, z)}{(1+z)^3 D_A(z)^2} \int \frac{ldl}{(2\pi)} P_m(k_l, z) J_2(l\theta), \quad (21)$$

where $k_l = l/[D_A(z)(1+z)]$, J_2 is the second order Bessel function of the first kind, $\theta = R/D_A(z)$ is the separation angle, $\rho_m(z)$ is the matter density at redshift z , $b_h(M, z)$ is the halo bias at mass M and redshift z and $P_m(k, z)$ is the matter power spectrum at the halo redshift z . Finally, the total excess surface density profile is given by

$$\Delta\Sigma(R) = \Delta\Sigma_{1h}(R) + \Delta\Sigma_{2h}(R) \quad (22)$$

When clusters are identified from photometric surveys, a fraction f_{mis} of clusters are "mis-centered", i.e. their observed center differs from their true one, such that the offset radius R_{mis} between the observed and true center follows a given statistical distribution $P(R_{\text{mis}})$ within the stack (see Appendix E.1 for more details). Miscentering is generally a big concern ([Sommer et al. 2022](#); [Melchior et al. 2017](#); [Zhang et al. 2019](#); [Johnston et al. 2007](#)), so cluster lensing-based studies require accurate knowledge of the miscentering fraction and offset distribution, to correct the one-halo term prediction. However, as we will see later in Section 6, we found that miscentering is not a worry for the analysis of DC2 lensing profiles, given the analysis choices that are made through the paper (i.e. a $R > 1$ Mpc radial cut, see Section 5).

Besides, the background source selection may cause contamination of the source sample by cluster member galaxies ([Varga et al. 2019](#)), which dilutes the signal in the innermost region, depending on the radial fraction of member galaxies $f_{\text{cl}}(R)$. This effect could be corrected at the model level in Eq. (22) by applying a boost factor coefficient ([McClintock et al. 2019](#)), or using more sophisticated methods, e.g. $P(z)$ decomposition ([Varga et al. 2019](#)). Similar to miscentering, it was found to be negligible in our analysis based on the radial distribution of cosmoDC2 halo member galaxies included in the source sample after applying source selection on photometric redshift datasets (see Appendix E.1/Section 6). For the overall dilution of the cluster signal, we rather use a simple model proposed by [Simet et al. \(2017\)](#), which we detail in Section 6.3.1.

The collapsed dark matter halos are not expected to be spherical, due to the non-spherical initial density peaks from which they form, and also due to their complex individual accretion history in the cosmic web ([Sheth et al. 2001](#)). The underlying dark matter halos are shown to have complex triaxial structures in simulations ([Jing & Suto 2002](#); [Schneider et al. 2012](#); [Despali et al. 2014](#)) and from the observation of their member galaxies ([Binggeli 1982](#)) or their weak lensing shear field ([Oguri et al. 2003, 2010](#)). In this analysis, we will consider stacks of individual cluster lensing profiles, which allow us to average over individual cluster morphologies. Then, for a stack of N_{obs} clusters, identified within the i -richness bin ($\lambda_i < \lambda < \lambda_{i+1}$) and the j -redshift bin ($z_j < z < z_{j+1}$). As for the cluster count, the selection function is essential to predict the average cluster lensing profile for a stack of detected clusters. It is however not straightforward, since the purity of the cluster finder induces

that the cluster catalog is contaminated by "spurious" detections; It first can be pure random noise in the detection (not associated with structures), but also spurious objects, such as improperly identified structures along the line-of-sight, or unmatched fragments of larger clusters. These structures will inevitably introduce a coherent (positive) lensing signal, which should be accounted for in the modeling. For simplicity, we will consider in this work that the purity quantifies the fraction of random "false" detections only. Let us define $N_{\text{obs}}^{\text{true}}$ as the number of *true* halos that are effectively detected by the redMaPPer cluster finder in a given redshift-richness (i.e. the number of redMaPPer clusters that were geometrically matched to the true underlying halo population, see Section 4.4.2), and $N_{\text{obs}}^{\text{false}}$ denotes for the contaminants in the cluster sample (similarly, redMaPPer clusters that were not geometrically matched). We can write

$$\langle \widehat{\Delta\Sigma} \rangle_{\text{obs}} = \frac{1}{N_{\text{obs}}} \left(\sum_{k=1}^{N_{\text{obs}}^{\text{true}}} \widehat{\Delta\Sigma}_k + \sum_{k'=1}^{N_{\text{obs}}^{\text{false}}} \widehat{\Delta\Sigma}_{k'} \right). \quad (23)$$

We consider that spurious detections will provide a null lensing signal on average, then, by turning the false detection contribution (second term in Eq. (23)) to zero, we get that the predicted stacked excess surface density profile is given by

$$\Delta\Sigma_{ij}(R) = \frac{1}{N_{ij}} \int_{z_i}^{z_{i+1}} dz \int_{\lambda_j}^{\lambda_{j+1}} d\lambda \int_{m_{\text{min}}}^{+\infty} dm \times \frac{d^2 N(m, z)}{dz dm} c(m, z) P(\lambda|m, z) \Delta\Sigma(R|m, z). \quad (24)$$

where we introduce the $c(m, z) \sim N_{\text{obs}}^{\text{true}}/N^{\text{true}}$, i.e. the fraction of true detected halos to the underlying halo population. However, we recall that it is a strong assumption that "spurious" redMaPPer detections (very low massive galaxy halos, misidentified structures along the line-of-sight, etc.) induce a null lensing signal. Separate contributions from redMaPPer spurious detections and "true" halos to the stacked lensing profiles could be estimated from forward simulations, by properly simulating the lensing signal of very low mass halos or directly using a match between the underlying population of halos and the redMaPPer clusters to investigate the excess of lensing due to the identified "false" detections. This was not explored extensively in the literature and this is not the purpose of this work, so we will keep using the aforementioned assumption.

Alternatively to using the stacked profile directly, one can use the inferred mean mass of the clusters within the richness-redshift bin (obtained from the profile) to investigate the cluster scaling relation (we will give more details in Section 3). For this purpose, using the same arguments as above, the mean mass can be modeled by

$$M_{ij} = \frac{1}{N_{ij}} \int_{z_i}^{z_{i+1}} dz \int_{\lambda_j}^{\lambda_{j+1}} d\lambda \int_{m_{\text{min}}}^{+\infty} dm \times \frac{d^2 N(m, z)}{dz dm} c(m, z) P(\lambda|m, z) m. \quad (25)$$

In this analysis, either equation (24) or (25) will be used to model the cluster lensing information, in combination with cluster counts, to constrain the mass-richness relation (see next section).

3. Mass-richness relation inference

Different methodologies are used in this paper to infer the cluster scaling relation. We first review the Bayesian framework, by presenting the different likelihoods and priors for the inference.

3.1. Likelihoods for cluster observables and priors

To infer the scaling relation parameters in Eq. (2) and in Eq. (3), we draw the posterior distribution

$$\mathcal{P}(\theta|\text{data}) = \frac{\mathcal{L}(\text{data}|\theta) \times \pi(\theta)}{\mathcal{L}(\text{data})}. \quad (26)$$

In the above, "data" refers to either stacked lensing profiles (referred to as WLp in the following), inferred stacked lensing masses (referred to as WLM), or cluster count (referred to as N), as well as a combination of abundance and lensing information. Next, we review the likelihood functions that we will use independently or in combination.

3.1.1. Cluster count likelihood

We consider the cluster count likelihood (Hu & Kravtsov 2003)

$$\mathcal{L}_N \propto |\Sigma_N|^{-1/2} \exp \left[-\frac{1}{2} [N - \widehat{N}]^T \Sigma_N^{-1} [N - \widehat{N}] \right], \quad (27)$$

where \widehat{N}_k are measured cluster count in Figure 2, N_k is the modeling in Eq. (6) and Σ_N is the cluster count covariance matrix given in Eq. (7). This likelihood (accounting for Poisson shot noise and SSC) has been used in Abbott et al. (2020); Costanzi et al. (2019); Sunayama et al. (2023).

We use the best-fitted selection function Φ (the fitting procedure is detailed later, in Section 4.3) and the Tinker et al. (2010) model for the mean halo bias in the cluster count covariance in Eq. (7).

3.1.2. Stacked cluster mass likelihood

The cluster mass-richness relation can also be inferred using the information from mass estimates (McClintock et al. 2019; Abbott et al. 2020; Lesci et al. 2022). We review later in Section 5 how we obtained stacked cluster mass estimates from the measured stacked excess surface density profiles in the cosmoDC2 simulation. Then, the stacked mass likelihood is given by

$$\mathcal{L}_{\text{WLM}} \propto |\Sigma_{\text{WLM}}|^{-1/2} \exp \left[-\frac{1}{2} \Delta \log_{10} M^T \Sigma_{\text{WLM}}^{-1} \Delta \log_{10} M \right], \quad (28)$$

where $\Delta \log_{10} M_k = \log_{10} M_k - \log_{10} \widehat{M}_k$, $\log_{10} M_k$ is the mass prediction that is given in Eq. (25) and $\Sigma_{\text{WLM}} = \text{diag}[\sigma^2(\log_{10} \widehat{M}_k)]$ is the stacked cluster mass covariance matrix, taken to be diagonal.

3.1.3. Stacked lensing profile likelihood

Another option to constrain the mass-richness relation is to use the stacked excess surface density profiles directly (Murata et al. 2019; Park et al. 2023; Sunayama et al. 2023). Compared to the two-step approach consisting of first fitting the stacked lensing masses from stacked excess surface density profiles and then constraining the cluster scaling relation using the likelihood in Eq.(28), this one-step method has more flexibility to incorporate

several systematic effects associated with the lensing measurement, such as the miscentering, the projection of correlated and uncorrelated structures around the clusters, cluster member contamination and the shape of non-spherical clusters. However, the one-step approach represents a significant computing challenge, since it requires to marginalize over many theoretical and observational effects (Aguena et al. 2023).

The likelihood for stacked excess surface density profiles, denoted \mathcal{L}_{WLP} , is given by

$$\mathcal{L}_{\text{WLP}} \propto |\Sigma_{\text{WLP}}|^{-1/2} \exp \left[-\frac{1}{2} [\Delta\Sigma - \widehat{\Delta\Sigma}]^T \Sigma_{\text{WLP}}^{-1} [\Delta\Sigma - \widehat{\Delta\Sigma}] \right], \quad (29)$$

where $\widehat{\Delta\Sigma}$ correspond to the stacked excess surface density profiles estimated in Eq. (10), and the prediction $\Delta\Sigma$ in each richness-redshift bin is given by Eq. (24). Σ_{WLP} are covariance matrices, obtained by bootstrap resampling as presented in Section 2. We assume that the covariance matrices are diagonal since the offset elements are extremely noisy (Phriksee et al. 2020).

Then, the total likelihood is obtained by combining the weak lensing likelihood (either \mathcal{L}_{WLM} or \mathcal{L}_{WLP}) with the count likelihood \mathcal{L}_{N} , to constrain the scaling relation parameters. Let us note that the way the lensing and counts likelihood are combined neglects any possible covariance between the two (Costanzi et al. 2019) showed that the cross-correlation between the abundance and the weak lensing inferred quantities is consistent with zero, at least reasonably negligible in our analysis). To compute the posterior in Eq. (26), we use the priors given in Table 1 (second column).

3.2. Softwares

For this work, we have used several DESC software tools, currently in development as part of the DESC pipeline for analyzing the upcoming LSST data. For the extraction of the cluster, halo, and background galaxy catalogs from the DC2 dataset, we used the DESC package GRCatalogs⁷, as well as Qserv⁸, an open source (Massively Parallel Processing) SQL database system designed originally to host the LSST data. For the estimation of the stacked lensing profiles, we used the DESC Cluster Lensing Mass Modeling (CLMM⁹, Aguena et al. (2021)) code that provides various tools for the estimation of cluster lensing profiles as well as halo modeling. We used the Core Cosmology Library¹⁰ (CCL, Chisari et al. (2019)) for the prediction of the halo mass function, the halo bias, and the concentration-mass relations. The combination of all these codes was performed in the LSSTDESC/CLCosmo_Sim repository¹¹.

The PySSC¹² package (Lacasa et al. 2018; Gouyou Beauchamps et al. 2022) was used to compute the binned S_{ij} terms for the cluster count covariance in Eq. (7). The inference of cluster scaling relation parameters was performed using the implementation of the Markov Chain Monte Carlo (MCMC) in the emcee package (Foreman-Mackey et al. 2013), and we use getdist (Lewis 2019) for visualization. Finally, we also make use of the Minuit¹³ minimizer (James & Roos 1975), much faster than an MCMC, to fit the stacked cluster mass in the two-step procedure (see details in Section 5.3).

⁷ <https://github.com/LSSTDESC/gcr-catalogs>

⁸ <https://qserv.lsst.io/index.html>

⁹ <https://github.com/LSSTDESC/CLMM>

¹⁰ <https://github.com/LSSTDESC/CCL>

¹¹ https://github.com/LSSTDESC/CLCosmo_Sim

¹² <https://github.com/fabienlacasa/PySSC>

¹³ <https://scikit-hep.org/iminuit/about.html>

4. Datasets

In this section, we detail the datasets we use in this paper. We first present Data Challenge 2, from which the cosmoDC2 extra-galactic catalog (Kovacs et al. 2022) and the catalog of clusters detected by redMaPPer (Rykoff et al. 2014) are derived.

4.1. The Data Challenge 2 (DC2)

DC2 is a vast simulated astronomical dataset covering 440 deg², that is designed to help develop and test the pipeline and analysis tools of DESC for interpreting the LSST data (see full details in Abolfathi et al. (2021)).

The DC2 galaxy catalog is built upon the OUTERIM N-body (gravity-only) simulation (Heitmann et al. 2019). Each dark matter halo has been identified by a friend-of-friend (FoF) halo finder and has been assigned a mass M_{FoF} (the sum of the individual dark matter particles associated between them) and a spherical overdensity mass M_{200c} (by fitting an NFW profile to each dark matter particle distribution). The galaxies inside halos were drawn from the Galacticus semi-analytic model of galaxy formation (Benson 2012), and were painted onto dark matter halos using GALSAMPLER (Hearin et al. 2020). The derived galaxy properties include stellar mass, morphology, spectral energy distributions, broadband filter magnitudes, and host halo information. The weak lensing shears and convergences at each galaxy position were estimated by a ray-tracing algorithm applied to the past light-cone particles in the simulation. We note that the performance of the ray-tracing procedure is degraded in the innermost regions of cluster fields (typically at $R \leq 1$ Mpc); this resolution effect was observed in Korytov et al. (2019) and discussed in Kovacs et al. (2022) for galaxy-galaxy lensing and cluster-galaxy lensing, and we cover in more details in Section 5.2 how we handled this issue in our data analysis pipeline.

4.2. The cosmoDC2 extra-galactic catalog and photometric redshift add-on catalogs

The cosmoDC2 extra-galactic catalog (Korytov et al. 2019; Kovacs et al. 2022) contains ~ 2.26 billion galaxies, making the inventory of ~ 550 properties of the "true" galaxies (i.e. true magnitudes in the six LSST bands, true redshift, true shapes, etc.) as well as the ray-tracing quantities per galaxy (shear and convergence) up to a magnitude depth of 28 in the r -band and to redshift $z \sim 3$. In that sense, it represents an ideal LSST dataset (there is no extinction from dust, stars, etc., only galaxies).

This work also uses two cosmoDC2 photometric redshift add-on catalogs, produced by DESC using representative established approaches in the literature, namely FlexZBoost (Izbicki & Lee 2017)¹⁴ and BPZ (Bayesian Photometric Redshifts, Benítez (2011)¹⁵). FlexZBoost is an empirical, machine-learning-based technique that has been shown to yield highly accurate conditional photometric redshift density estimates in prior work (Schmidt et al. 2020). FlexZBoost uses spatially overlapping data from LSST and accurate spectroscopic redshift information to estimate the conditional redshift distribution $p(z|m)$, based on LSST photometric bands m . BPZ is a template-based fitting method, which formulates a likelihood of the galaxy's observed colors from a set of redshifted Spectral Energy Distribution (SED) models. This approach includes valuable information such as the shape of the redshift distribution and galaxy type.

¹⁴ <https://github.com/rizbicki/FlexCoDE>

¹⁵ https://github.com/LSSTDESC/rail_bpz

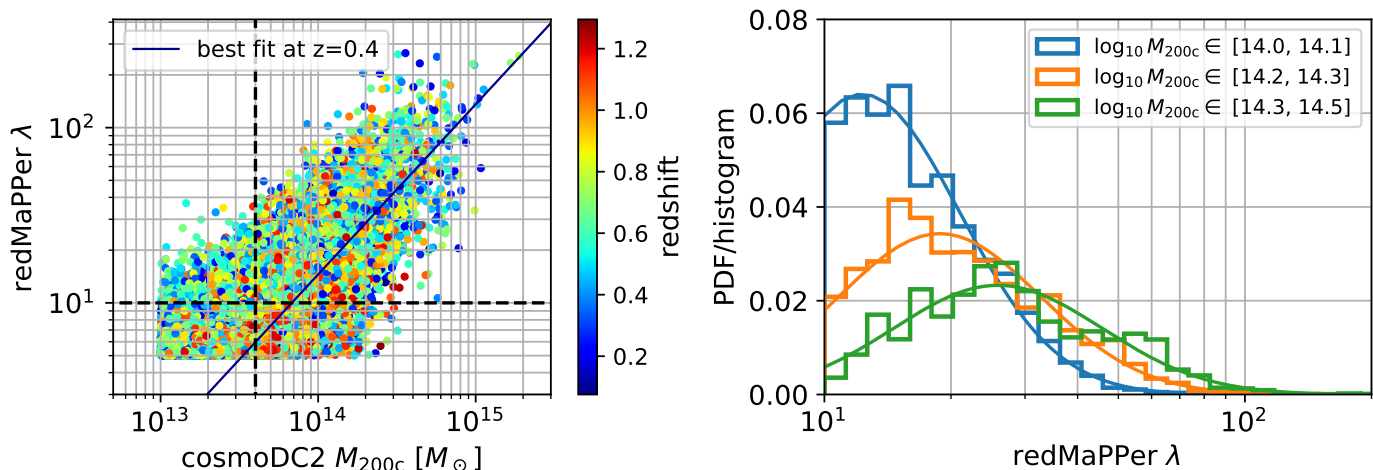


Fig. 1. Left: cosmoDC2 halo M_{200c} masses (from the simulation) versus the redMaPPer cluster richnesses. The points are colored with the redMaPPer cluster redshift. The full line is the best-fitted mean richness-mass relation in Eq. (2) at $z = 0.4$. The dashed lines represent the low mass and low richness cut used on the cosmoDC2-redMaPPer matched catalog for the fit of the fiducial scaling relation. Right: Histogram of richnesses in bins of mass, and best-fit probability distributions $P(\ln \lambda | M, z)$ from Eq. (1) (full lines) for the different mass bins.

The DC2 simulation suite has two limitations that affect the photometric redshift estimates. First, the simulation data does not model spectroscopic surveys and their galaxy selection. In cosmoDC2, FlexZBoost was trained with a complete subsample of galaxies that extended to $i < 25$. This depth extends beyond the range where spectroscopic surveys can be assumed to be complete (although it remains representative of LSST depth). In consequence, the accuracy of the photometric redshift estimates derived using the FlexZBoost technique should be considered optimistic. Second, the color-redshift space of the modeled galaxies is not continuous but discrete due to the details of the mock photometry construction (Korytov et al. 2019)¹⁶. While template-fitting techniques can be expected to be less affected by incomplete calibration data, they rely more heavily on accurate SED models¹⁷. This non-physical discreteness in the data therefore leads to inaccurate fits for template-fitting methods, which correctly assume that the spectral energy distribution of galaxies changes smoothly with redshift¹⁸. In that sense, the accuracy of the DC2 BPZ redshift should be considered pessimistic.

We expect realistic photometric redshift estimates to fall somewhere between the optimistic FlexZBoost and the pessimistic BPZ DC2 runs, although it is likely to be closer to FlexZBoost given these unphysical effects.

4.3. The redMaPPer cluster catalog

As mentioned in the introduction, galaxy clusters can be identified through their member galaxies from galaxy catalogs such as cosmoDC2. The redMaPPer cluster finder (Rykoff et al. 2014), which identifies clusters through the presence of red-sequence

¹⁶ Specifically, a very low-resolution internal dust model was used, which led to additional "breaks" in some galaxy spectra, especially at high redshift.

¹⁷ While template-fitting techniques can be expected to be less affected by incomplete calibration data, they are much more agnostic than empirical techniques, since they rely more heavily on accurate SED models, compared to the specificity of the calibration dataset.

¹⁸ This is not a fundamental limitation of template-fitting techniques but rather arises due to the strong underlying a priori assumptions that empirical techniques impose on the generalization of the conditional $p(z|m)$ between the calibration and LSST data.

Parameters	Priors	$p \pm \Delta p$
$\ln \lambda_0$	$\mathcal{U}(0, +\infty)$	3.35 ± 0.01
μ_z	$\mathcal{U}(-2, 2)$	0.06 ± 0.08
μ_m	$\mathcal{U}(0, +\infty)$	2.23 ± 0.05
$\sigma_{\ln \lambda_0}$	$\mathcal{U}(0, +\infty)$	0.56 ± 0.01
σ_z	$\mathcal{U}(-2, 2)$	-0.05 ± 0.04
σ_m	$\mathcal{U}(-2, 2)$	0.10 ± 0.02

Table 1. Second column: Prior we use in this analysis, we also consider $\sigma_{\ln \lambda | m, z} > 0$. Third column: Posterior means for the four parameters of the scaling relation, by using individual dark matter halo masses and redMaPPer richnesses.

galaxies, has already been widely used on SDSS (Abdullah et al. 2020) and DES (Abbott et al. 2020) and has been run on cosmoDC2 (see Ricci et al. in prep for details). We note that by using the cosmoDC2 galaxy catalog for the redMaPPer run, the resulting cluster catalog is not affected by any atmospheric and instrumental effects. The redMaPPer catalog provides galaxy cluster positions, redshifts, and richnesses (calculated as the sum of membership probabilities of galaxies around the cluster) along with per-cluster membership galaxies catalog, for 880,000 clusters within $5 < \lambda < 270$ and $0.1 < z < 1.15$. In addition to redMaPPer, other detection methods have been applied to find clusters of galaxies in the cosmoDC2 data (WaZP, Aguena et al. (2021); AMICO, Bellagamba et al. (2018); YOLO-CL, Grishin et al. (2023)) whose corresponding catalogs are, or will soon be, available within DESC.

4.4. The matched cosmoDC2 halo - redMaPPer cluster catalog

To infer the *true* cluster scaling relation, we have associated the redMaPPer detected clusters to the cosmoDC2 dark matter halo catalog using the DESC software CIEvaR¹⁹. The association is based on membership matching (see e.g. Farahi et al. (2016)),

¹⁹ <https://github.com/LSSTDESC/CIEvaR>

where we use the member galaxies²⁰ of detected redMaPPer clusters and of cosmoDC2 halos, respectively; Each halo is associated with all the detected clusters with which it shares galaxies and vice versa. The one-to-one catalog is then obtained by considering associated systems (redMaPPer cluster-cosmoDC2 halo) with the highest "membership fraction" (overlap between the cosmoDC2 halo and redMaPPer cluster member galaxies) and keeping only the pairs that are associated with one another (two ways match). The matching procedure was obtained considering $M_{\text{FoF}} > 10^{13} M_{\odot}$ for the dark matter halo catalog and $\lambda > 5$ for the redMaPPer cluster catalog. We checked that this gives identical mass-richness relation parameters as applying a cut $M_{200c} > 10^{13} M_{\odot}$ directly. The redMaPPer-cosmoDC2 masses and richness are displayed in Figure 1 (left panel).

Then, each redMaPPer cluster with richness λ_k is assigned a "true" spherical overdensity mass $M_k = M_{200c,k}$. We show in Figure 1 (left panel) the matched redMaPPer cluster-cosmoDC2 halo catalog objects in the mass-richness plane, color-coded according to their redshifts.

4.4.1. The fiducial mass-richness relation

From the cosmoDC2-redMaPPer matched catalog we can infer a "fiducial" scaling relation. We consider the clusters with $\lambda > 10$ (horizontal dashed line), as well as $M > 4 \times 10^{13} M_{\odot}$ (vertical dashed line) and with $0.2 < z < 1$. We consider the "fiducial" likelihood given by

$$\mathcal{L}_{\text{fid}} = \prod_{k=1}^{N_{\text{tot}}} P_{\ln \lambda_k > \ln 10}(\ln \lambda_k | M_k, z_k), \quad (30)$$

where $P(\ln \lambda_k | M_k, z_k)$ is given in Eq. (1) for the k -th cluster-halo match, and the subscript denotes truncated Gaussians with $\ln \lambda_k > \ln \lambda_{\text{min}} = \ln(10)$. We use the emcee package (Foreman-Mackey et al. 2013), and we use flat priors inspired from Murata et al. (2019) as listed in Table 1 (second column). The best-fitted fiducial relation using Eq. (30) is shown in Table 1 (third column). These values can serve as a reference against which we will compare the results obtained using cluster weak lensing and abundance.

The low mass/richness cuts applied to the matched catalog are deliberately conservative. These cuts are chosen to ensure that the *completeness* of the redMaPPer cluster catalog (see Section 4.4.2) does not influence the inference of the cluster scaling relation. In Appendix B, we examine the impact of alternative cuts, motivated by the modeling of the mass-richness relation used in this work. While this topic warrants further investigation, for this study, we adopt the fiducial values listed in Table 1 (third column).

We show, over-plotted in black in the left panel of Figure 1, the mean of the scaling relation for the best-fitted parameters, at $z = 0.4$. The right panel in Figure 1 shows the normalized histograms of redMaPPer richness in 3 different bins of masses (and within the fill redshift range $z \in [0.2, 1]$), where we over-plot the best-fitted probability density function $P(\lambda | m_{\text{center}}, z_{\text{center}})$, where z_{center} and m_{center} are the center of each redshift-mass bins. We see that the predicted distribution matches well the observed one.

²⁰ For the member galaxies, we used respectively the redMaPPer member galaxies for each cluster (i.e. the output of redMaPPer) and cosmoDC2 galaxies flagged as "members" for each cosmoDC2 dark matter halo in the simulation.

4.4.2. The redMaPPer selection function

To properly model cluster counts, we need to account for the selection function of the catalog (see e.g. Euclid Collaboration et al. (2019); Lesci et al. (2022)). It reflects the fact that the cluster finder algorithm may miss a fraction of true clusters of galaxies (completeness), as well as detect "false" clusters that are not related to underlying collapsed dark matter structures (purity). We recall the parametrization of the selection function given by (see e.g. Aguena & Lima (2018))

$$\Phi(\lambda, m, z, z_{\text{obs}}) = \frac{c(m, z)}{p(\lambda_{\text{obs}}, z_{\text{obs}})}, \quad (31)$$

where $c(m, z)$ is the *completeness* and $p(\lambda_{\text{obs}}, z_{\text{obs}})$ is the *purity*. The selection function usually accounts for the true halo redshift z and the observed redshift z_{obs} of the detected galaxy cluster, which may differ from the halo true redshift. Here, we consider $z = z_{\text{obs}}$ for simplicity otherwise it should account for the conditional distribution $P(z_{\text{obs}} | z)$.

From the matched catalog, we can disentangle between the effects of purity and completeness, within narrow mass-redshift-richness bins. The measured completeness \widehat{c}_{ij} in the mass and redshift bins $[m_i, m_{i+1}]$ and $[z_j, z_{j+1}]$ and the measured purity \widehat{p}_{kl} in the richness and observed redshift bins $[\lambda_k, \lambda_{k+1}]$ and $[z_{\text{obs},l}, z_{\text{obs},l+1}]$ are given by (see e.g. Euclid Collaboration et al. (2019))

$$\widehat{c}_{ij} = \frac{N_{\text{match},ij}^{\text{halos}}}{N_{\text{tot},ij}^{\text{halos}}} \quad \text{and} \quad \widehat{p}_{kl} = \frac{N_{\text{match},kl}^{\text{halos}}}{N_{\text{obs},kl}^{\text{clusters}}}, \quad (32)$$

where $N_{\text{tot},ij}^{\text{halos}}$ is the total number of halos in the ij mass-redshift bin, $N_{\text{obs},kl}^{\text{clusters}}$ is the number of redMaPPer clusters in the kl richness-redshift bin. The quantity $N_{\text{match},ij}^{\text{halos}}$ (respectively $N_{\text{match},kl}^{\text{halos}}$) is the number of halos that have been matched to redMaPPer clusters in the ij mass-redshift bin (respectively in the kl richness-redshift bin). We model the *observed* completeness \widehat{c}_{ij} and purity \widehat{p}_{kl} with continuous smoothed step functions, so they can be included in the count/lensing formalism as detailed in Section 2. The performances of the DC2 redMaPPer cluster catalog are analyzed in detail in Ricci et al. (in prep.). We note that the redMaPPer cluster catalog is complete at the 80% level for $M_{200c} > 10^{14} M_{\odot}$, with a small redshift dependency, and is pure at the $> 90\%$ level for $\lambda > 12$. Hence, we will cut the catalog at $\lambda > 20$ in the following.

5. Cluster data vectors for the count and weak lensing analyses

From this dataset, we now move to the construction of the data vectors that will serve for the inference of the redMaPPer cluster mass-richness relation. For the stacking strategy we employ, we have considered the redshift bin edges $z_i = \{0.2, 0.3, 0.4, 0.5, 0.6, 0.7, 0.8, 1\}$ and the richness bin edges $\lambda_i = \{20, 35, 70, 100, 200\}$.

5.1. Cluster number count

We show in Figure 2 the measured count of redMaPPer clusters as a function of richness, for different redshift bins. Error bars correspond to Poisson shot noise, i.e. $\sigma(N) = \sqrt{N}$. We see clearly that at higher richness, there are fewer clusters. We recall that the observed redshift-richness abundance is linked to the underlying cluster scaling relation, halo mass function, and selection function we present afterward.

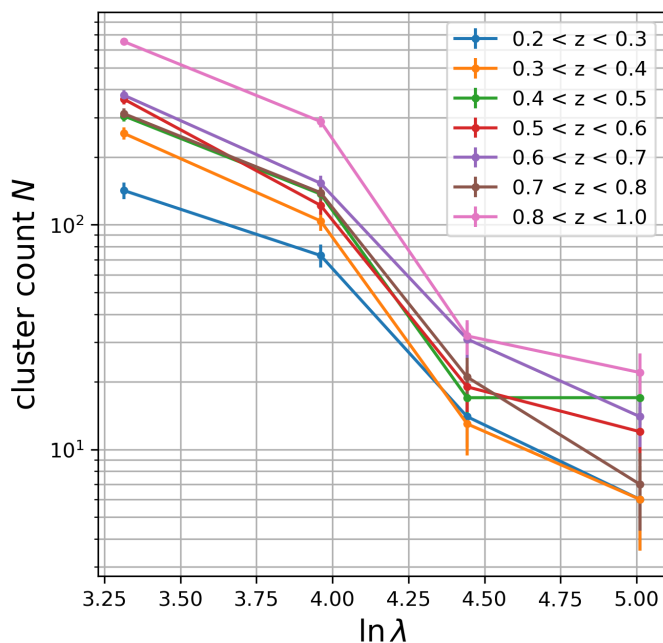


Fig. 2. Measured count of redMaPPer cluster as a function of richness (the dots are placed at the center of richness bins), for different redshift bins.

5.2. Stacked excess surface density profiles

Source selection is first based on a cut $r < 28$ in the r -band and $i < 24.25$ in the i -band, to reach the effective number density of galaxies $n_{gal} \approx 25 \text{ arcmin}^{-2}$ to be comparable to that will be used in the context of LSST after 10 years of data (Chang et al. 2013). The recovered cosmoDC2 redshift distribution is shown in black in Figure 9. In this work, we construct each galaxy's lensed ellipticity ϵ_{obs} from (i) its intrinsic shape ϵ_{int} , (ii) the evaluation of shear and convergence at the galaxy's location through Eq. (8). As a result, observed galaxy ellipticities are not affected by shape measurement errors. The shape noise on each galaxy ellipticity component is $\sigma_{SN} = 0.25$, comparable to what was found in the literature (Chang et al. 2013).

Then, for each cluster in the redMaPPer catalog, we extract the source catalog in a circular aperture of $R = 10 \text{ Mpc}$, applying the source selection $z_s > z_l + 0.2$, where z_s is the true cosmoDC2 galaxy redshift, and z_l is the redMaPPer cluster redshift. We will present in Section 6 the different methodologies we adopt for source selection when using photometric redshifts. For each stack of N_l clusters, we consider the 10 log-spaced radial bins from 0.5 Mpc to 10 Mpc, and we estimate the stacked lensing profile using Eq. (10).

The corresponding excess surface density profiles are displayed in Figure 3 as a function of the distance to the cluster center in Mpc, for different richness bins (colors) and the different redshift bins (columns). At fixed richness, we do not see a particular trend in redshift at scales larger than 1 Mpc, denoted by the vertical dashed lines in Figure 3.

However, for $R < 1 \text{ Mpc}$, we see that the stacked lensing profiles are progressively attenuated in the innermost regions. This attenuation has already been observed in the galaxy-galaxy lensing (Korytov et al. 2019) and cluster-galaxy lensing (Kovacs et al. 2022) in DC2 and is associated with the limited resolution of the ray tracing to compute the lensing shear and convergence at each galaxy position, as a consequence, we chose to use only the $R > 1 \text{ Mpc}$ region for each stack in the analy-

sis. This choice is valid over the full richness and redshift range. However, this also means we cannot use the innermost regions with the largest SNR values. This intrinsic limitation will limit the cluster-related forecasts of what could be achieved with the LSST data. We show in Figure 4 the signal-to-noise ratio of some excess surface density profiles for a low (resp. high) redshift bin in the top panel (resp. bottom panel). In the considered redshift range, the SNR oscillates between 2 and 13 for the low redshift bin, and between 0.5 and 8 for the high redshift bin. The profiles in the last richness bin have the lowest SNR, due to the low statistics in these bins (~ 10 times fewer clusters than in the first richness bin). Let us note that the stacking strategy allows us to significantly increase the SNRs, since SNRs of individual cluster excess surface density profiles (not shown here) range from 0.1 to 3 (to go from stacked profile SNRs to individual profile ones, a good approximation is to rescale them by $1/\sqrt{N_l}$).

5.3. Stacked cluster masses

As mentioned before, alternatively to directly use the stacked profiles for the weak-lensing information, one may instead use the cluster masses inferred from those profiles. To do so, for each k -th stack in each redshift-richness bin, we infer the *effective* cluster mass $\log_{10} \widehat{M}_k$ and its corresponding error $\sigma(\log_{10} \widehat{M}_k)$ that matches the stacked lensing profile $\widehat{\Delta\Sigma}_k$. We fit a dark matter density profile (e.g. NFW) to each stacked lensing profile using the Minuit²¹ minimizer (James & Roos 1975), much faster than an MCMC. We ensured that the recovered mass and error from Minuit coincide at the $< 0.1\sigma$ level with the mean mass and errors inferred from an MCMC procedure.

After fitting the stacked profiles within the radial range $1 < R < 3.5 \text{ Mpc}$ with an NFW dark matter density profile using a Duffy et al. (2008) concentration-mass relation (these modeling choices are referred to as the "baseline" analysis, see Section 3 for more details), we show in Figure 5 (left panel) the inferred stacked cluster masses as a function of richness, for the different redshift bins (colors). Error bars on the y-axis correspond to the statistical error we obtain from our fitting procedure of the cluster mass, while the x-axis error is the dispersion of richness values in each bin. We see that the amplitude increases with richness, as expected.

For validation, we have compared the recovered lensing mass to the mean *true* mass in each redshift-richness bin in Figure 5 (right panel), where the true masses are obtained by matching the redMaPPer cluster catalog to dark matter halos. We see a clear correlation between recovered and true mass with scatter around the one-to-one correspondence.

6. Results

All ingredients are now in place to perform the analysis of the scaling relation of redMaPPer clusters. We start in Section 6.1 by presenting the setup that will serve as our baseline analysis. Section 6.2 discusses how the modeling choices for the halo density and mass-concentration relation affect the results while Section 6.3 focuses on observational systematic effects, and more

²¹ We use `minuit.migrad()` and `minuit.minos()` sequentially to (i) determine the best-fit cluster mass $\log_{10} M$ and (ii) compute the asymmetric error bars $\log_{10} M_{-\sigma_-}^{+\sigma_+}$. In Eq. (28), we adopt a Gaussian likelihood with symmetric errors, for which we use the mean error $(\sigma_+ + \sigma_-)/2$. However, asymmetric errors can be more accurately modeled using, for example, a split normal distribution.

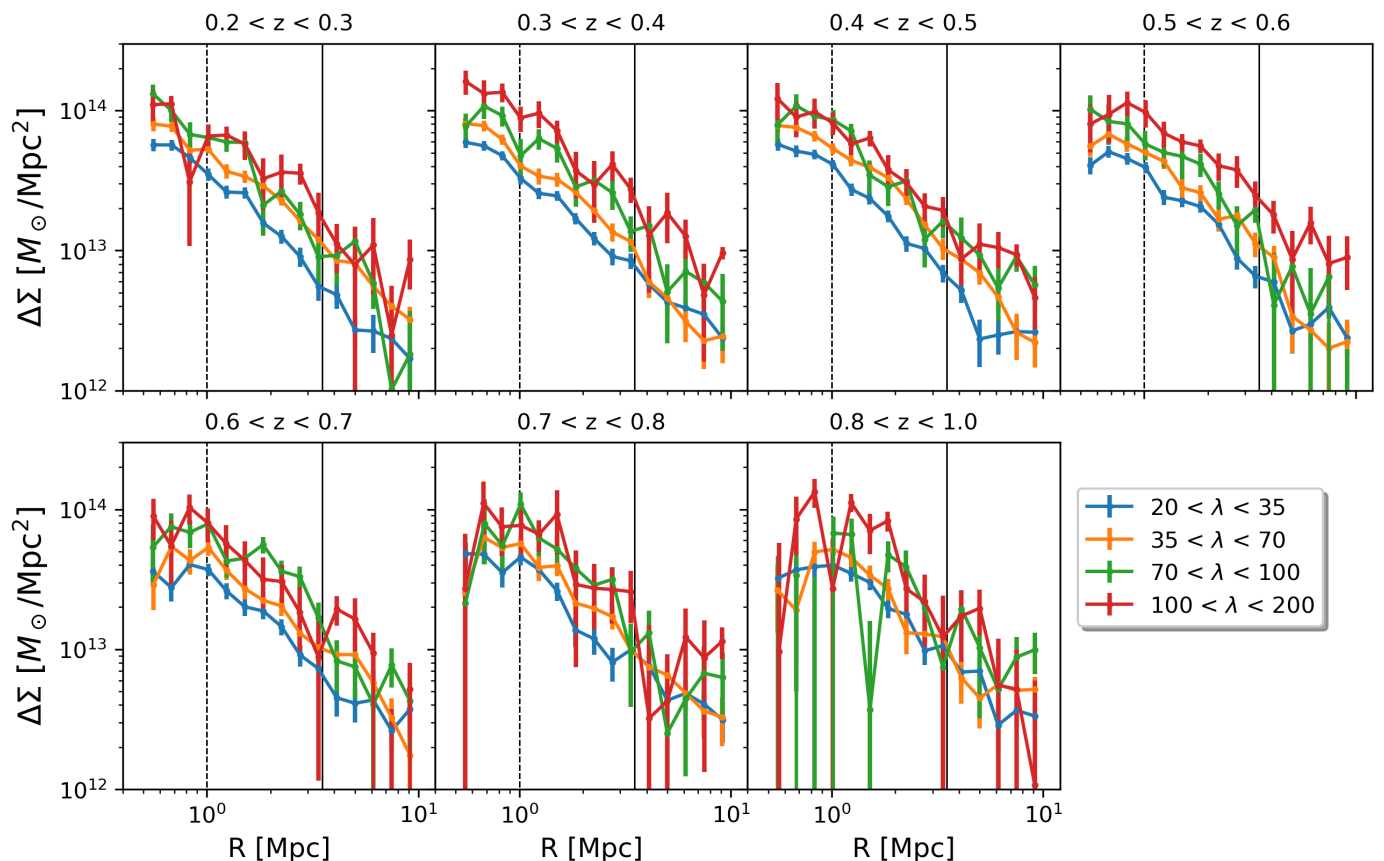


Fig. 3. Stacked excess surface density profile as a function of the distance to the cluster center, for different richness bins (colors) and different redshift bins (from top left to bottom right). The error bars are the diagonal elements of the bootstrap covariance matrices. The black dashed vertical line (resp. black filled vertical line) represents the $R > 1$ Mpc cut (resp. $R < 3.5$ Mpc cut).

specifically on the source photometric redshifts and on the shear-richness covariance. Table 2 lists the tables and figures of the different study cases.

6.1. Baseline weak lensing/count analysis

We model the per-cluster excess surface density $\Delta\Sigma(R|m, z)$ using a three-dimensional dark matter density profile given by

$$\rho(r) = \rho_s \left(\frac{r}{r_s} \right)^{-1} \left(1 + \frac{r}{r_s} \right)^{-n}, \quad (33)$$

which is the Navarro-Frank-White (Navarro et al. 1997) for $n = 2$. Then, $r_s = r_{200c}/c_{200c}$ is the scale radius, and ρ_s is the scale density²². We use a concentration mass-relation from Duffy et al. (2008) (see 6.2.1 hereafter). The stacked profile in each richness-redshift bin is given in Eq. (24), by using the Despali et al. (2015) halo mass function and the best-fit redMaPPer selection that we present in Section 4.3, as well as the scaling relation in Eq. (1).

We restrict the fitting to $1 < R < 3.5$ Mpc. The typical value of $R_{\max} = 3.5$ Mpc is inspired by Lee et al. (2018); Giocoli et al. (2021); Cromer et al. (2022); Murray et al. (2022); Bocquet et al. (2024), and is typically the distance beyond which the two-halo

²² From Eq. (20), the scale density is given by

$$\rho_s = \frac{200}{3} \frac{c_{200c}^3}{f(c_{200c})} \rho_c(z) \quad \text{where} \quad f(x) = \ln(1+x) - x/(1+x). \quad (34)$$

term increasingly dominates the cluster lensing signal and cannot be neglected (this choice is discussed further in Appendix C and later in the text).

We show in Figure 6 (left panel) the 68% and 95% credible intervals on the cluster scaling relation when using separately the cluster abundance likelihood (blue, Eq. (27)), stacked lensing profiles (dashed red, Eq. (29)) or stacked lensing masses (green, Eq. (28)). The vertical/horizontal bars represent the "fiducial" values of the redMaPPer cluster scaling relation inferred in Section 4.4.1. We see that abundance provides tighter constraints but has different degeneracies than lensing (stacked profiles of stacked masses). We see that contours have characteristic degeneracies and a strong degree of overlap, so we can combine them. We also note that the posteriors are fairly compatible with the fiducial constraints at the $1-2\sigma$ level.

The different degeneracy directions between abundance and lensing contours provide tight final constraints on the scaling parameters when combined²³. By combining abundance with lensing, we obtain the posteriors in Figure 6 (right panel) either with stacked profiles (blue full lines) or stacked masses (orange filled contours) (for scale, we show in black - left panel - the joint abundance and lensing profiles posterior). We see that using either masses or profiles provides roughly the constraints with the same precision and the errors on the mean scaling parameters ($\ln \lambda_0$, μ_z and μ_m) are reduced by a factor of ~ 7 , where the errors on the scatter terms ($\sigma_{\ln \lambda_0}$, σ_z and σ_m) are reduced by a

²³ Again, we recall that the cosmological parameters are fixed to the DC2 values in the MCMC.

Analysis	Section	Numerical values	Posterior distribution
Fiducial relation	Section 4.4.1	Table 1	-
Baseline	Section 6.1	Table A.1 (first block)	Figure 6
Modeling - $c(M)$ relation	Section 6.2.1	Table A.1 (second block)	Figure 7 (left panel)
Modeling - dark matter density profile	Section 6.2.2	Table A.1 (third block)	Figure 7 (right panel)
Observational - photometric redshifts	Section 6.3.1	Table A.1 (fourth block)	Figure 10 (left panel)
Observational - shear-richness covariance	Section 6.3.2	Table A.1 (fifth block)	Figure 10 (right panel)

Table 2. List of the different study case of the result section Section 6. We indicate to the reader where to find the dedicated subsections, tables, and figures.

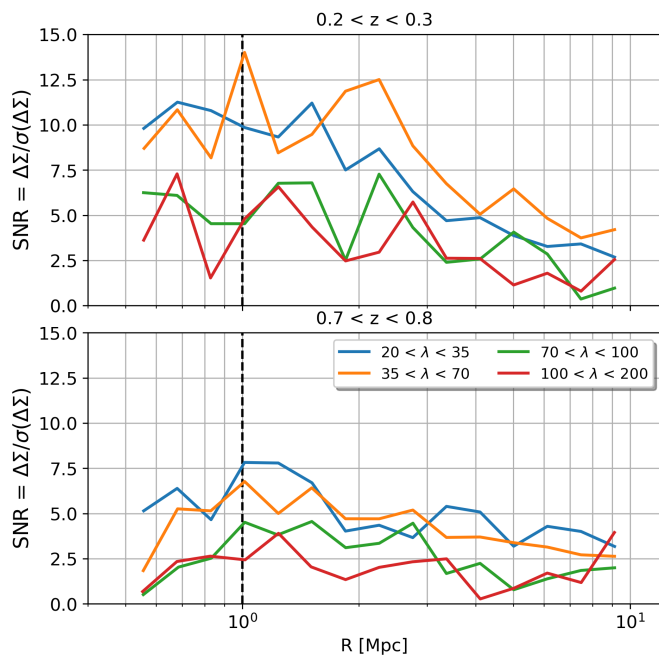


Fig. 4. Signal-to-noise ratio of the stacked excess surface density profiles, for two different richness bins (top and bottom panel) and different richness bins (colors).

factor of $\sim 3 - 4$. One-dimensional posteriors obtained from our joint lensing and abundance likelihood fairly recover the fiducial values at the $< 2\sigma$ level, however, we see a $> 2\sigma$ tension with the projected posterior on $\mu_z - \sigma_z$.

We check whether the stacked lensing profiles in the last redshift bin are impacted by the ray-tracing shear resolution beyond 1 Mpc despite our conservative radial cut, since the attenuation maximal increases with redshift, thus being maximal in the last bin. To do that we remove the last redshift bin in the estimation of the posterior (from abundance and lensing profiles). This result is presented in black dashed lines in Figure 6 (right panel), providing compatible results with our baseline analysis, with wider error bars (the last redshift bin contains 30% of the full cluster catalog). The baseline provides us with a sanity check of our lensing and count pipeline, that fairly compares to the "fiducial" constraints of the redMaPPer mass-richness relation, where residual systematics inherent to our analysis such as the calibration of the halo mass function, the selection function uncertainties may induce some bias in the recovered parameters.

We also examine in Appendix C the impact of alternative R_{\max} cuts on the scaling relation parameters. We find that using the full radial range available (up to $R_{\max} = 10$ Mpc) without modeling the two-halo term yields comparable results to the baseline $R_{\max} = 3.5$ Mpc cut, with small biases ($< 1\sigma$) and sim-

ilar error bars. This is due to the noisy lensing measurements (low SNR) at larger scales, which reduce the impact of the two-halo term and do not provide additive information. However, the two-halo term cannot be neglected for larger datasets. For consistency with other works that focus on the one-halo term, we will continue to use the $R_{\max} = 3.5$ Mpc cut in this study.

The best-fit scaling relation parameters for our baseline analysis are shown in A.1 (first block, we will put the values, means, and errors on the parameters of the scaling relation obtained from count and lensing in Appendix A). In the following, we will always use the combination of lensing (either mass or profiles) and count to probe the underlying cluster scaling relation, thanks to their complementarity in the parameter space.

6.2. Impact of modeling choices

The inference of the cluster scaling relation is affected by several systematic effects, arising from the numerous degrees of freedom in the modeling of the cluster observables. In this paper, we focus on the systematics associated with the modeling of the weak lensing signal. Choosing a particular mass distribution model instead of another may impact the cluster lensing mass, and have a non-negligible impact on the mass-richness relation. We will focus on the one-halo regime, i.e. below $R = 3.5$ Mpc, which is more sensitive to the proper halo properties (cluster mass, concentration) compared to the two-halo regime, more sensitive to cosmological quantities through the power spectrum and the halo bias.

6.2.1. Concentration-mass relation

The cluster density profile is usually modeled using an extra concentration parameter, labeled as c_{200c} , which can be fitted jointly with the cluster mass.

On one side, we can fit the weak lensing stacked masses in each richness-redshift jointly with the mean concentration, and we use them in the mass likelihood in Eq. (28). In Figure 7 (left panel), the purple dashed contours represent the constraints on the scaling relation parameters when using the joint count/mass likelihood, that is in reasonable agreement with the fiducial constraints.

On the other side, cosmological simulations indicate that both cluster concentration and mass are statistically correlated, and this correlation can be quantified via a fitting formula called a concentration-mass relation – labeled as $c(M)$. Such a $c(M)$ (see e.g. Diemer & Kravtsov 2014; Duffy et al. 2008; Prada et al. 2012; Bhattacharya et al. 2013; Diemer & Joyce 2019) relation can reduce the number of free parameters in cluster-based studies, and thus improve constraints on the other relevant parameters. For example, our baseline choices use the Duffy et al. (2008) relation, which was calibrated with N-body simulations

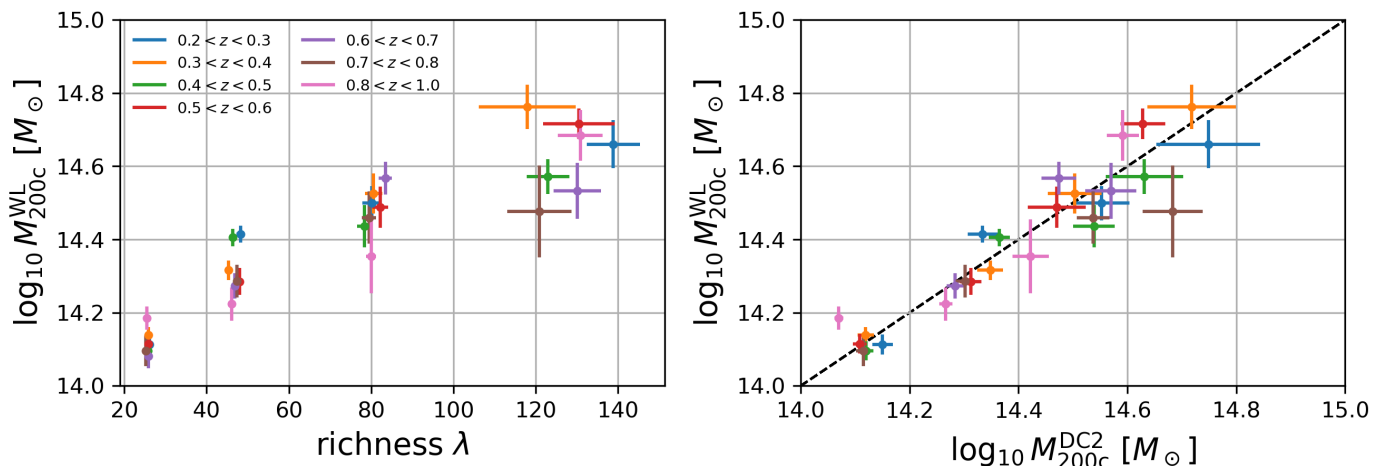


Fig. 5. Left: stacked lensing mass as a function of mean richness within the stack, the different colors correspond to the different redshift bins. Right: Stacked lensing masses as a function of the DC2 matched masses from the cosmoDC2 dark matter halo catalog. The different colors correspond to the different redshift bins. The dashed line corresponds to $y = x$.

based on the 5-year WMAP cosmology (Komatsu et al. 2009), differing by at most 5% from the 7-year WMAP cosmology (Komatsu et al. 2011) used in cosmoDC2. The other relations examined in this section (Prada et al. 2012; Bhattacharya et al. 2013; Diemer & Kravtsov 2014) have been shown to accurately describe the relationship between halo masses and concentrations across various Λ CDM cosmologies.

To test the impact of $c(M)$ relation on the scaling relation parameters, we (i) fit the stacked masses using a $c(M)$ relation (where M denotes the mean stacked mass) (ii) use these stacked mass estimates in Eq. (28) (iii) combine with the count likelihood in Eq. (27) to infer the scaling relation parameters. In Figure 7, we show the constraints on the scaling relation parameters using different concentration-mass relations, that are fully consistent with the free-concentration case (dashed lines). The posteriors obtained with a fixed $c(M)$ relation provide the same level of correlation between parameters, moreover slightly decreasing the error bars since fewer parameters are free in the fitting procedure. We would expect the concentration choice to have a bigger impact in the inner regions $R < 1$ Mpc, which are not available due to ray-tracing resolution.

6.2.2. Modeling of the matter density profile

Besides the NFW parameterization, Einasto (1965) has derived an empirical profile that is shown to provide a slightly better fit in N-body simulations of galaxy clusters compared to NFW, especially at small scales over a broad range of halo masses and redshifts (Klypin et al. 2016; Sereno et al. 2016; Wang et al. 2020). The corresponding three-dimensional profile is given by

$$\rho^{\text{ein}}(r) = \rho_{-2} \exp\left(-\frac{2}{\alpha} \left[\left(\frac{r}{r_{-2}}\right)^\alpha - 1\right]\right), \quad (35)$$

where $r_{-2} = r_{200c}/c_{200c}$ and the ρ_{-2} is given in the footnote²⁴. In the above equation, α is the shape parameter. We use a typical

²⁴ The density ρ_{-2} is given by

$$\rho_{-2} = 200\rho_c(z) \frac{2}{3} \gamma^{-1} \left[\frac{3}{\alpha}, \frac{2}{\alpha} c_{200c}^\alpha \right] \frac{c_{200c}^3}{e^{2/\alpha}} \left(\frac{2}{\alpha} \right)^{\frac{3-\alpha}{\alpha}} \quad (36)$$

where γ is the lower incomplete gamma function.

constant value of $\alpha = 0.25$, but let us note that more sophisticated models incorporate mass, redshift, and cosmology dependence in α , that are observed in simulations (Gao et al. 2008), making α ranging typically from 0.15 to 0.3 with mass. Besides, although not considered in this work, Diemer (2023) has proposed a refined formula of the Einasto profile, as the original expression is not valid in the transition region where halos become dominated by newly accreting matter.

Less common, the Hernquist density model (corresponding to $n = 1$ in Eq. (33)) was used for instance in Buote & Lewis (2004); Sanderson & Ponman (2009) to model the mass density of X-ray-detected galaxy clusters, but has not been extensively used in the lensing literature.

Concentration-mass relations for the Einasto and Hernquist models have not been extensively studied in the literature, so we will consider the fit without assuming a particular $c(M)$ relation, thus privileging the count/mass cluster likelihood. We show in Figure 7 (right panel) the posterior distribution of the scaling relation parameters when considering the count/mass likelihood, respectively using the NFW (filled contours), the Einasto (full lines) or the Hernquist (dashed lines). The results are in perfect agreement with each other, likely due to the radial range we used in the fit, where profiles are similar, and start shaping differently at smaller scales.

So fitting the stacked cluster mass from 1 Mpc to 3.5 Mpc, where the one-halo regime is dominant and using either NFW, Einasto or Hernquist profile only is relevant, we have found that the inferred scaling relation is rather stable.

6.3. Observational systematic effects

We have addressed several possible sources of bias due to the uncertainty in the modeling of the cluster lensing observable. The other major source of bias in cluster lensing analyses arises from data, i.e. from the calibration of galaxy shapes (Hernández-Martín et al. 2020), of the redshift distribution of the background galaxy sample (Wright et al. 2020), and contamination of the source galaxy sample with foreground galaxies (Varga et al. 2019).

Using the cosmoDC2 catalog, we use the true shapes of galaxies (i.e. only accounting for the intrinsic shape and the local

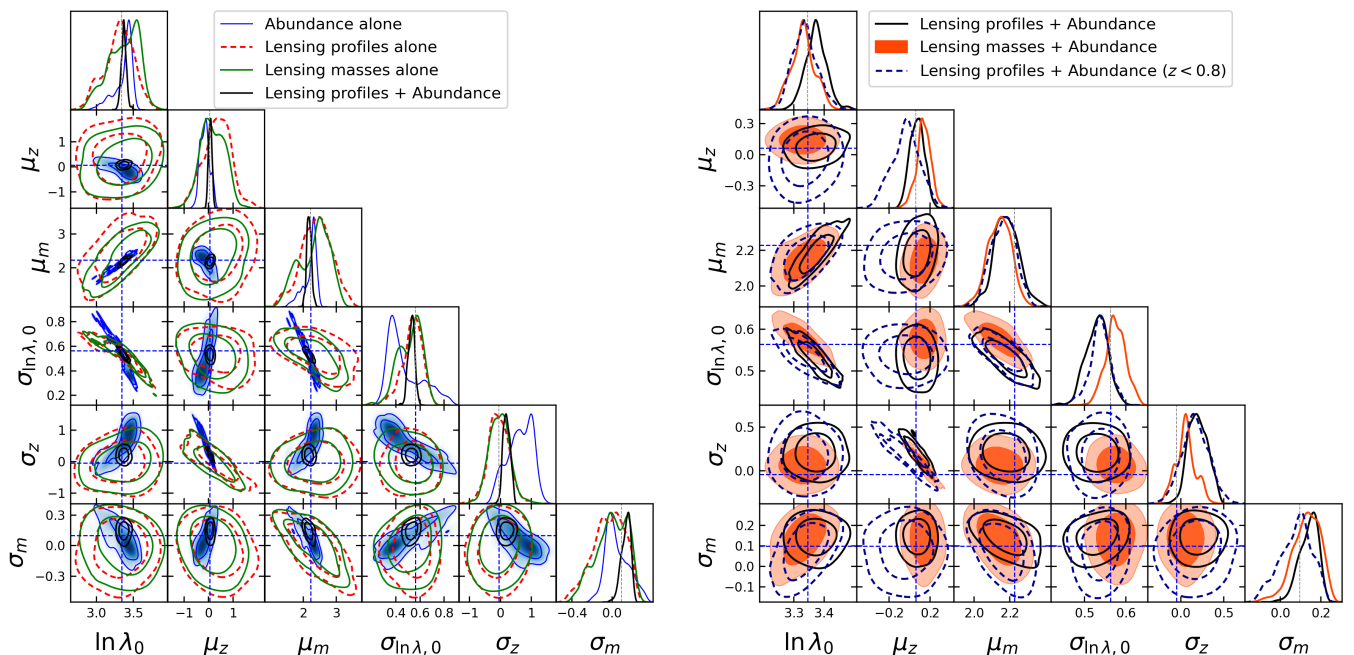


Fig. 6. Left: Posterior distribution of the scaling relation parameters using abundance alone (blue), lensing profiles alone (dashed red), or masses alone (green, full lines). The joint abundance and lensing profiles posterior is displayed in black. Right: Posterior distribution of scaling relation parameters when combining abundance and lensing profiles (blue, full lines) and combining abundance and cluster masses (orange-filled contours). The dashed contours are obtained by removing the last redshift bin for both abundance and lensing.

shear), so cannot investigate the effects of shape measurement errors with this dataset.

We also checked that miscentering was a minor issue given the radial cuts of the analysis. Using the matched catalog between redMaPPer clusters and cosmoDC2 dark matter halos, we study the miscentering fraction f_{mis} and the distribution of cluster center offsets $P(R_{\text{mis}})$ as discussed in Section 2.3, by assuming that R_{mis} is the 2D distance between the cosmoDC2 halo and the redMaPPer cluster centers. From the offset distribution, we measured that $f_{\text{mis}} \approx 0.15$, and that the miscentering distribution is well described by a Gamma distribution (McClintock et al. 2019) with $\sigma_{\text{mis}} = 0.12$ Mpc. Using the miscentering formalism presented in E.1, we find that the bias with respect to a perfectly centered profile when using the redMaPPer offset distribution is at most 1% at $R = 1$ Mpc, and 0.25% at $R = 2$ Mpc. For simplicity, since the computation of the miscentering term is computationally demanding, we will neglect this contribution and consider a 1% systematic bias in our analysis originating from miscentering.

We will also not discuss the effect of contamination in detail. Source selection based on photo- z redshift may cause contamination of the source sample by cluster member galaxies when cluster member galaxies are misidentified and considered as background galaxies. Unlensed member galaxies contaminating the source sample dilute the lensing signal (Varga et al. 2019; McClintock et al. 2019). As described in Appendix E.2, the contamination was found to be largely negligible when using our photo- z -based source selection, combined with our conservative $R > 1$ Mpc cut.

From this, among all the observational systematics effects mentioned above, this section more specifically focuses on the impact of the calibration of the background galaxy photo- z redshift distribution on the cluster scaling relation (§6.3.1) and on the impact of shear-richness covariance (§6.3.2).

6.3.1. Source galaxy photo- z redshifts

In the previous Section 6.1 and Section 6.2, we have used the true galaxy redshifts to compute the geometrical lensing weights w_{ls}^{geo} . With imaging data, each source galaxy behind clusters has assigned photo- z redshift distribution, derived from the galaxy magnitudes measured in several optical bands. The uncertainty in the measured redshift can be accounted for in the lens-source geometrical weights in Eq. (11).

In this section, we test the impact of using BPZ (Benítez 2011) and FlexZBoost (Izbicki & Lee 2017) algorithms on the inference of the cluster scaling relation. For that, we modified the source selection, which is now based on photo- z quantities. Figure 8 shows the mean photometric (and dispersion) redshift as a function of the true cosmoDC2 redshift (we do not apply any photo- z quality cut). As FlexZBoost provides robust estimates up to $z = 3$, BPZ provides more dispersed results, and biased estimates above $z \sim 2$. The increased dispersion of BPZ estimates at higher redshifts is not unexpected, as the model photometry in the simulation included a non-physical dust feature in some SEDs at high redshift that were not present in the SED templates used to compute theoretical fluxes by BPZ, which induced a bias and increased dispersion.

As discussed in Section 4, none of these estimations are realistic due to (i) the deep selection of the training sample up to $i < 25$ for FlexZBoost, the results of which should be considered optimistic, and (ii) the "discreteness" in the color-redshift space of the modeled galaxies (Korytov et al. 2019), negatively impacting the performance of BPZ. Updated redshifts are currently being produced by the collaboration. These updated redshifts were not available at the time of this work, so we proceeded with the first version of the photo- z catalogs. The actual LSST data will most likely fall between the pessimistic BPZ and optimistic FlexZboost runs we used. By considering both approaches, we will be able to bracket the impact of photo- z on the results.

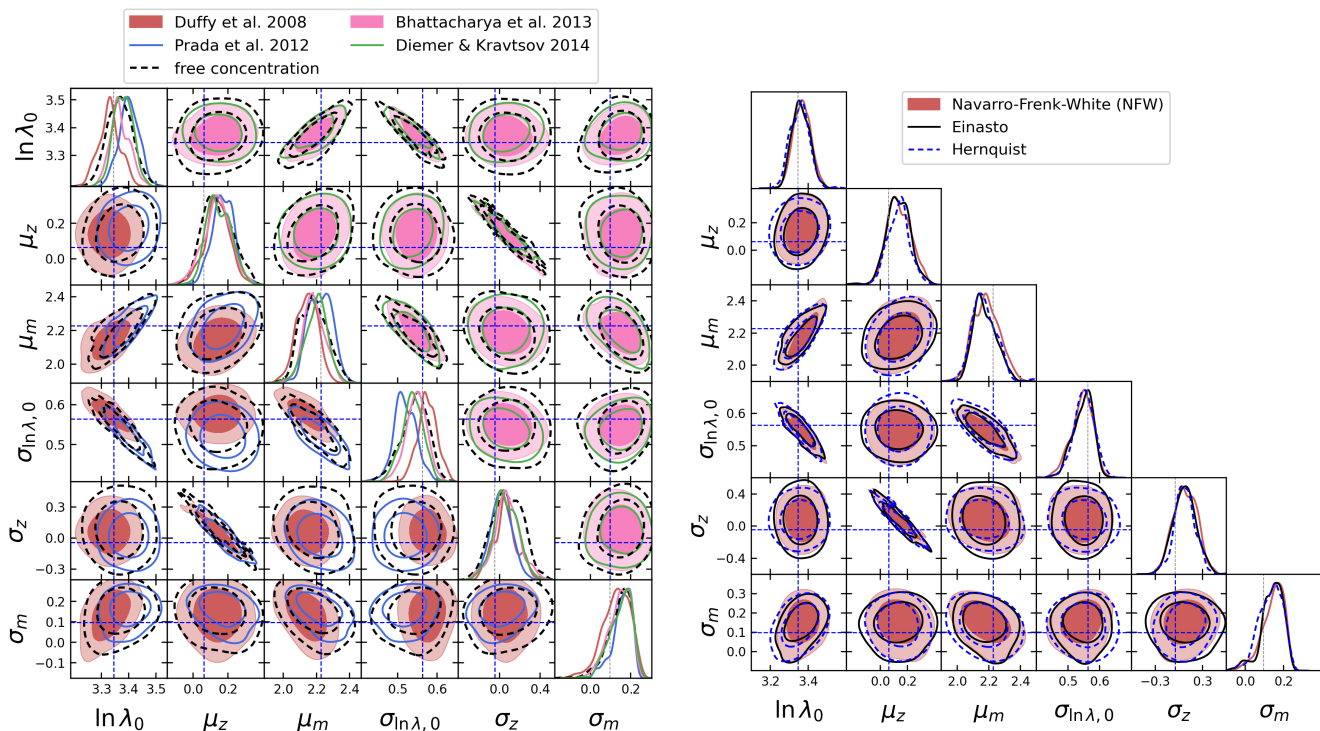


Fig. 7. Left: Posterior distribution of the scaling relation parameters using count/mass likelihood. The concentration-free case is shown with the dashed lines, the other contours are obtained using various concentration-mass relations from the literature. Right: Posterior distribution of the scaling relation parameters using count/mass likelihood, without using a concentration-mass relation, and using different modeling of the cluster density profile, namely NFW (red filled contours), Einasto (full lines), Hernquist (dashed lines).

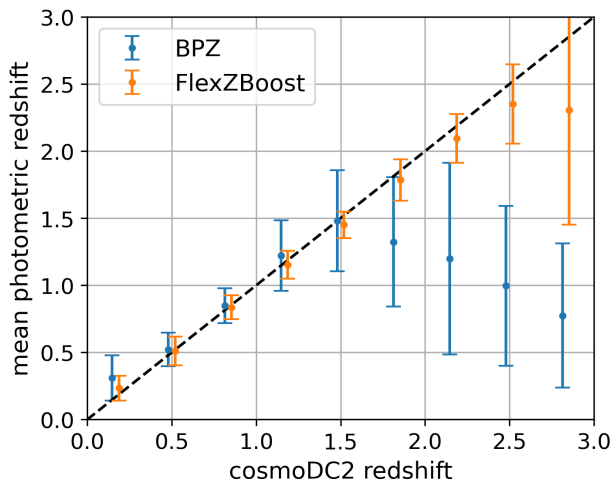


Fig. 8. Mean photometric redshift against true cosmoDC2 redshift for BPZ and FlexZBoost methods.

For the source sample selection, we use simultaneously two cuts based on (i) the photo- z redshift mean, such as $\langle z_s \rangle > z_l + 0.2$ and (ii) the probability density function with $P(z_s > z_l) > 0.8$, where

$$P(z_s > z_l) = \int_{z_l}^{+\infty} dz_s p(z_s), \quad (37)$$

is the probability for a galaxy with photo- z redshift distribution to be located behind the cluster. In the above equation, $p(z_s)$ is the galaxy photo- z redshift distribution (obtained either from BPZ or FlexZBoost). Moreover, we do not apply any quality cut

on photo- z s, so we can test the robustness of the cluster scaling relation with respect to photo- z in the "worst" case scenario, i.e. with no mitigation of the impact of outliers on the final results. We show in Figure 9 (left panel) the distribution of *true* galaxy redshifts in cosmoDC2 after our magnitude cuts (in black). In the left panel, we show the background source sample after applying the $P(z_s > z_l)$ cut alone (in blue) and combining the $P(z_s > z_l)$ and mean redshift cuts (in orange) on FlexZBoost redshifts, for a redMaPPer cluster at redshift $z = 0.38$. We see that our photometric source selection remove efficiently the foreground and member galaxies. The same distributions are shown in Figure 9 (right panel) for BPZ redshifts.

We show in Figure 10 (left panel) the constraints on the scaling relation when considering photo- z redshifts either from BPZ or FlexZBoost. We have used the count/lensing profile likelihood, where we model the one-halo term by an NFW profile with a Duffy et al. (2008) concentration-mass relation, and we restrict the fit to the one-halo regime. Using BPZ (right panel, lower triangle plot, dashed contours), introduces a small negative bias of $\sim 1\sigma$ in the normalization of the scaling relation, as well as in the mass dependence compared to the true redshift case (filled contours).

We can also incorporate a simple model to account for the photo- z bias at the level of the modeling of the stacked lensing profile, as proposed by Simet et al. (2017). We add a common factor $(1 + b)$ to every lensing profile, that is fitted jointly with the scaling relation parameters, with flat prior $[-0.5, 0.5]$ for b . Adding a free parameter $(1 + b)$ increases the size of the posteriors as expected (red contours), and helps decrease the tension between the photo- z case and the true redshift case. We recover a negative bias $b = -0.02 \pm 0.03$, compatible with 0 at the 1σ level. For FlexZBoost (left panel, upper triangle plot), we

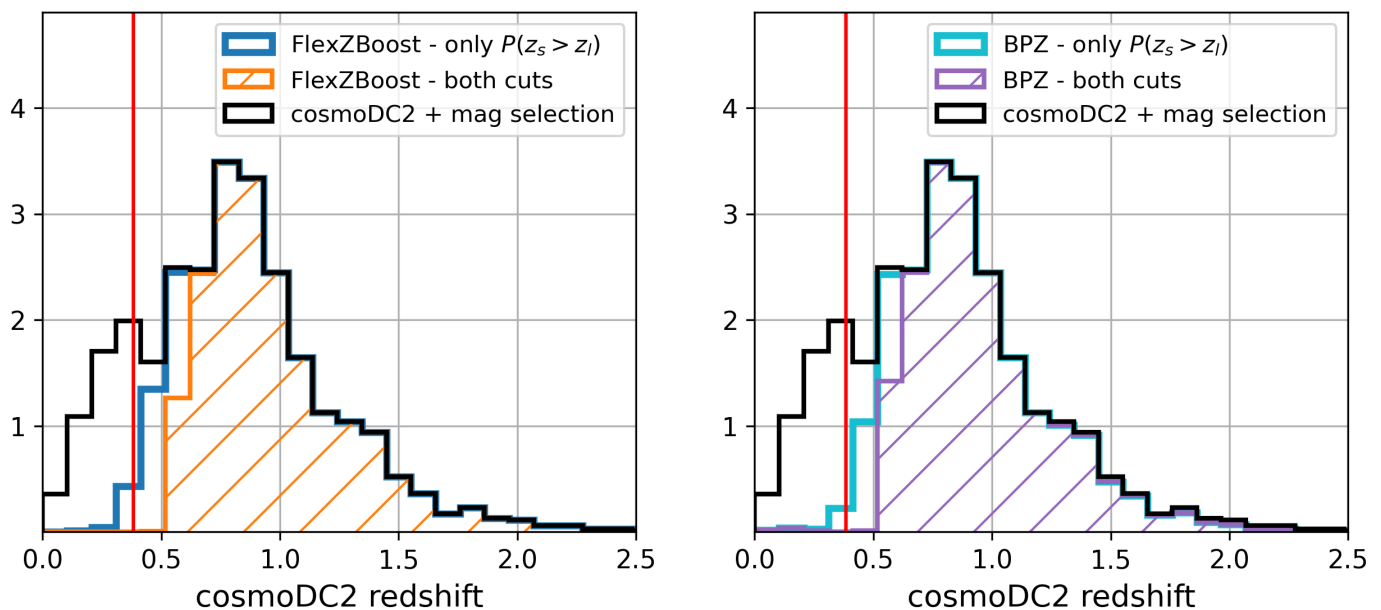


Fig. 9. Left: distribution of true cosmoDC2 redshifts after our magnitude cuts (black). The blue distribution represents the same distribution after a cut on the probability $P(z_s > z_l)$ using FlexZBoost photometric redshift, for a cluster at $z = 0.38$. The orange distribution is obtained after combining the $P(z_s > z_l)$ cut and the mean redshift cut. Right: same as left but for BPZ redshifts.

first see that without correction (dashed contours), constraints are fully compatible with the true redshift case (filled contours). Adding $(1+b)$, we recover $b = 0.02 \pm 0.03$ (empty contours), and error bars are increased without shifting significantly the posteriors.

6.3.2. Impact of shear-richness covariance

In this section, we discuss a systematic bias arising from selection biases in cluster finder algorithms. For optically selected clusters, one relatively unexplored category of cluster systematics is the covariance between the two cluster observables, first, the shear estimated from background galaxies and second the richness, as an outcome of cluster finders. This covariance was left unconstrained in previous cluster cosmology analyses as [McClintock et al. \(2019\)](#); [Abbott et al. \(2020\)](#). This property covariance can induce additive biases that cannot be mitigated with increased sample size and reduced shape noise ([Nord et al. 2008](#); [Evrard et al. 2014](#); [Farahi et al. 2018](#); [Wu et al. 2019](#)). To achieve percent-level mass calibration of clusters, this new category of systematics must be accurately and precisely quantified ([Rozo et al. 2014](#)). In this work, we follow the prescription of [Zhang et al. \(2024\)](#) in modeling and quantifying the systematic uncertainty induced by the property covariance of optically selected clusters on the cluster scaling relation.

We make a note of the difference between intrinsic and extrinsic covariance. In [Zhang et al. \(2024\)](#) the authors measured the intrinsic covariance of cluster weak lensing observables by encircling galaxies within a three-dimensional physical radius around the halo to measure the *true* richness and second, measured the integrated dark matter density around the halo. This *ground truth* measure of the covariance is caused by the galaxy assembly bias, the degree of which can be quantified by secondary halo properties (e.g. concentration, mass accretion rate, kinetic-to-potential energy ratio) that relate to the formation history of the cluster-sized halo. In this work, we measure the total covariance (intrinsic + extrinsic) using the redMaPPer cluster

finder to determine the observed richness and the galaxy shear as a proxy for the surface density. This realistic mock catalog introduces observational systematic such as photo- z redshift uncertainty ([Graham et al. 2017](#)) and shape noise ([Wu et al. 2019](#)) for the galaxy shear signal and projection and percolation effects ([Costanzi et al. 2018](#)), triaxiality bias ([Zhang et al. 2023](#)) and a set of other observational and modeling systematics ([McClintock et al. 2019](#)) related to a realistic cluster finder as redMaPPer.

Our goal is to model and correct for the systematic uncertainty of the estimated stacked lensing profiles in Eq. (10). From [Evrard et al. \(2014\)](#); [Aihara et al. \(2018\)](#); [Wu et al. \(2019\)](#); [Zhang et al. \(2024\)](#), the corrected stacked excess surface density profile is given by

$$\Delta\Sigma_{ij}^{\text{corr}} = \Delta\Sigma_{ij} + \ln(10) \frac{[\beta_1]_{ij}}{\mu_m} \times \langle \text{Cov}(\Delta\Sigma, \ln \lambda|m, z) \rangle_{ij}, \quad (38)$$

where $\Delta\Sigma_{ij}$ is given in Eq. (24), and $[\beta_1]_{ij}$ is the *average* logarithm slope of the [Despali et al. \(2015\)](#) halo mass function in the ij richness-redshift bin. For the latter, we compute $[\beta_1]_{ij}$ once before running MCMC, by using the fiducial cluster scaling relation, and we consider the denominator μ_m free. $\langle \text{Cov}(\gamma, \ln \lambda|m, z) \rangle_{ij}$ is the averaged shear-richness covariance (see calculation details in Appendix D), associated to potential selection bias in the cluster finder algorithms (the factor $\ln(10)$ is used to match the definition in [Evrard et al. \(2014\)](#)). In the latter, we will present the estimation of $\langle \text{Cov}(\gamma, \ln \lambda|m, z) \rangle_{ij}$, to be used in the estimation of the cluster scaling relation parameter.

While [Zhang et al. \(2024\)](#) observed a radially dependent covariance at small scales $R < R_{200c}$ due to cluster formation physics, because of the attenuation of the cluster lensing signal at small scales due to the ray tracing resolution, we will rather focus on the $R > 1$ Mpc scales. From mock-cluster studies analyzing selection effects such as [Wu et al. \(2022\)](#) and [Sunayama et al. \(2020\)](#) the total bias (intrinsic+extrinsic) is close to null at small scales and increases at larger scales for $R > R_{200c}$. For this reason, the covariance after applying the scale cut due to lensing

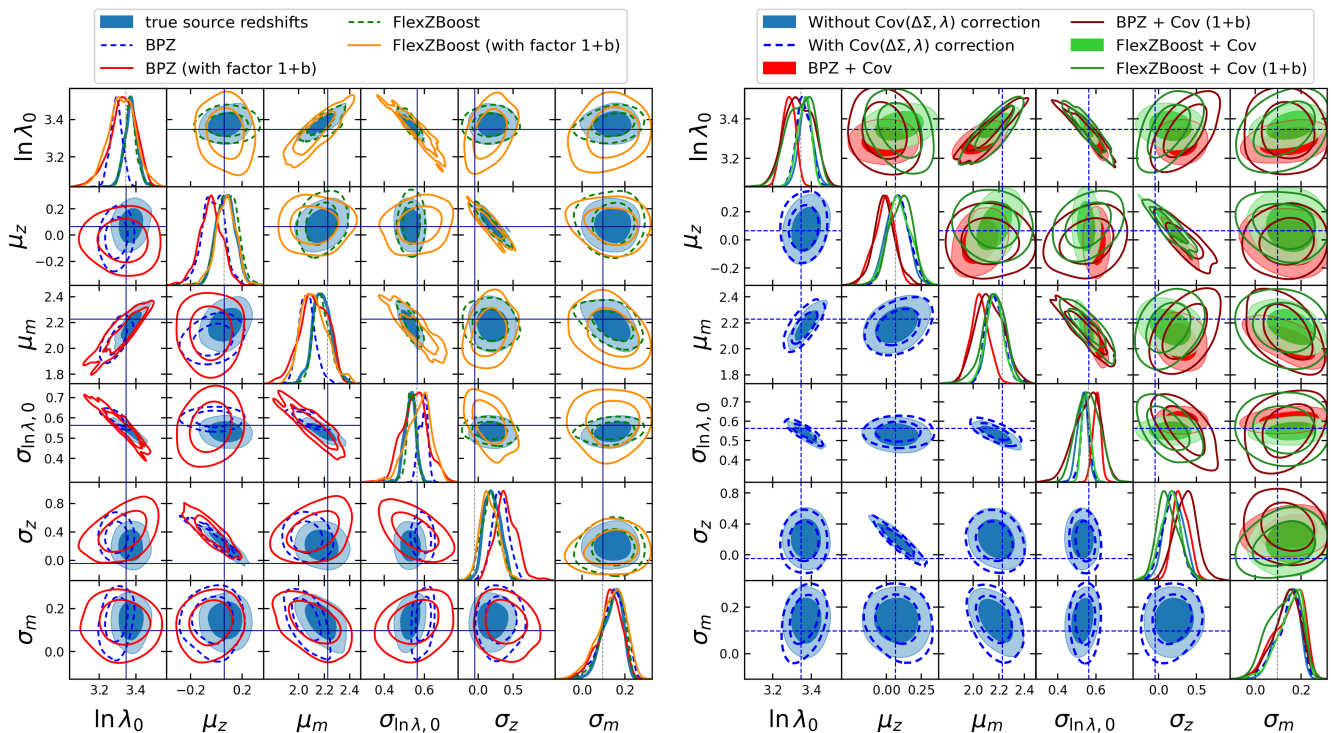


Fig. 10. Left: Posterior distribution of the scaling relation parameters. Lower triangle plot: The filled contours show the constraints when using true redshifts of source galaxies. Dashed contours are obtained when considering the BPZ photo- z redshifts. Empty contours are obtained using BPZ photo- z redshifts, after marginalizing over the $(1 + b)$ correcting factor, considered as a free parameter, used to correct from photo- z calibration issues. Upper plot: same as lower plot, but for FlexZBoost. Right: Posterior distribution of the scaling relation parameters with (red) and without (blue) the shear-richness covariance correction in Eq. (38).

attenuation may be sufficient for describing to impact of the total covariance.

We apply a Kernel Local Linear Regression (KLLR) (Farahi et al. 2022) to find the best fit local mean with mass as the independent variable and $\Delta\Sigma(R)$ and $\ln \lambda$ as the dependent variables. Specifically, the residuals of $\Delta\Sigma$ and $\ln \lambda$ are taken around their local mean quantities $\langle \Delta\Sigma | m, z, R \rangle$ and $\langle \ln \lambda | m, z \rangle$

$$\text{res}_{\Delta\Sigma}(m, z, R) = \Delta\Sigma - \langle \Delta\Sigma | m, z, R \rangle, \quad (39)$$

$$\text{res}_{\ln \lambda}(m, z) = \ln \lambda - \langle \ln \lambda | m, z \rangle \quad (40)$$

and the covariance is measured around the local residuals, i.e.

$$\langle \text{Cov}(\Delta\Sigma, \ln \lambda | m, z) \rangle_{ij} = \text{Cov}(\text{res}_{\Delta\Sigma}(m, z, R), \text{res}_{\ln \lambda}(m, z)). \quad (41)$$

It is important to note that as we remove the residual dependence of the mean mass on the covariance, the size of the covariance itself can still nonetheless be a function of (m, z) , i.e. the scatter and correlation are modeled as $\sigma_{\ln \lambda | M, z}(M, z)$ and $\sigma_{\Delta\Sigma | m, z}(m, z)$ and $r_{\ln \lambda - \Delta\Sigma | m, z}(m, z)$. For this reason, we test the covariance on small enough (m, z) bins that the scatter can be considered *homoskedastic*, or in other words approximated as a constant. In our benchmark tests, we choose to bin the covariance either in mass or redshift but not by both to retain enough statistical constraint, especially for high mass, low redshift bins with a low cluster count.

We plot the covariance merged by mass and binned in redshift in Figure 11. Visually we recognize a slight positive covariance in most bins. The same trend (not shown) can be said of a benchmark test for covariances binned by richness and merged between $z \in [0.2, 0.7]$ (it can be shown that the covariances in $z \in [0.7, 1.0]$ are null). To explicitly demonstrate the mass and redshift dependence we model the covariance as constant bias

across radius which we denote $b_{\text{Cov}}(M, z)$. The covariance trend with respect to richness (resp. redshift) is plotted in the right panel (resp. left panel) in Figure 12. From the figure, we see that the amplitude of the effect is smaller by a factor of 10 compared to the amplitude of the stacked lensing profile (i.e. 10^{12} versus 10^{13}).

To constrain the mass-richness relation accounting for this effect, we model the stacked excess surface density profile using Eq. (38). We propagate the error of the shear-richness covariance (error-bars in Figure 11) by adding the associated variance to the diagonal element of the total shear profile covariance matrices, multiplied by $[\log(10)\beta_1/\mu_m]^2$. We consider the stacked profiles estimated with true background source redshift, and we use the inference setup defined for our baseline analysis, by using a joint likelihood between counts and stacked lensing profile. The blue filled (resp. dashed) contours in Figure 10 (lower triangle panel), the posterior of the scaling relation parameters accounting for (resp. not accounting for) the shear-richness covariance correction calculated in Eq. (38). We see that the "corrected" posterior is shifted at the 0.5σ level compared to the baseline analysis. From this test, we have found that the impact of property covariance has a non-negligible impact on the scaling parameter inference, such as the size of the bias is much larger than what is obtained using FlexZBoost redshifts (see Section 6.3.1) and slightly less than what obtained with BPZ ones. Similar shifts to the true redshift case are obtained when considering adding FlexZBoost/BPZ photometric source redshifts, whose results are listed in Table A.1, fifth block (resp. green and red filled contours in Figure 10, upper triangle plot). The unfilled green and red contours in Figure 10 (upper triangle plot) show the combination of

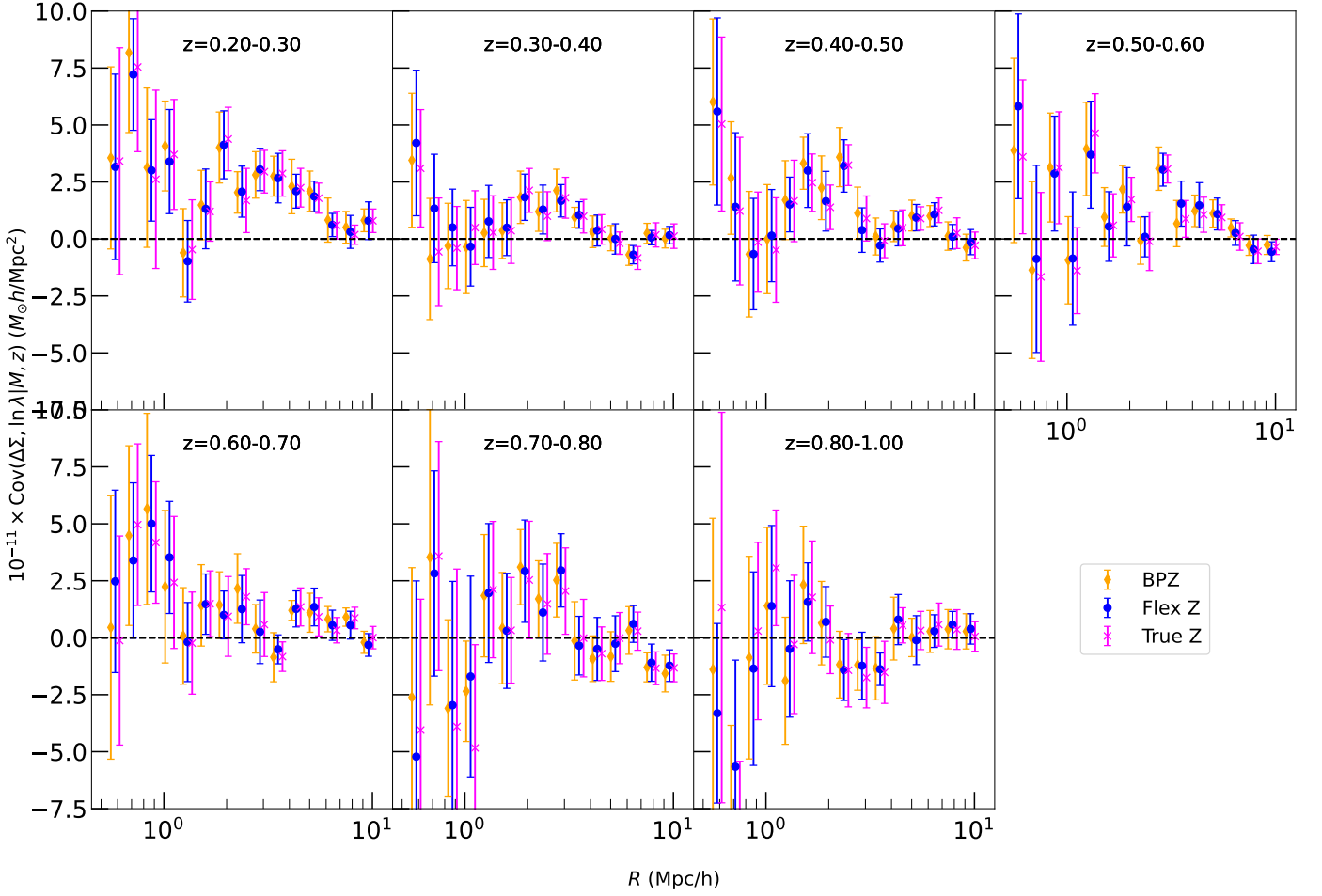


Fig. 11. Binned excess surface density-richness covariance in (41), as a function of the radius from the cluster center. We stack all clusters between $\lambda \in [20, 70]$ and subdivide by different redshift bins from the top left panel to the bottom right panel. The true redshift case is displayed in pink, the BPZ and FlexZBoost cases are represented in orange and blue, respectively.

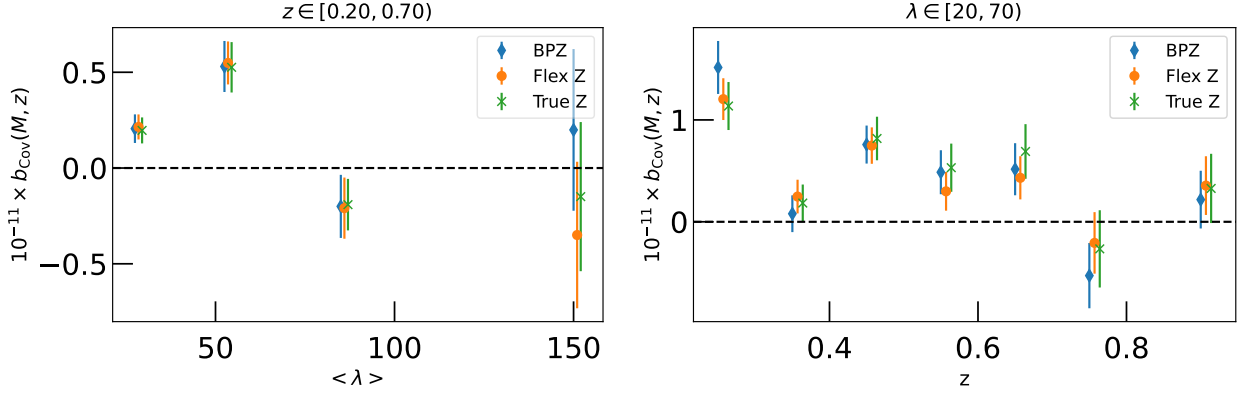


Fig. 12. The covariance (Eq. (41)) modeled as a constant bias term $b_{\text{cov}}(M, z)$ across radius when binned by richness (left) or redshift (right). The positive covariance at large scales at lower redshift and richness bins is consistent with expectations from projection effects.

the inclusion of selection bias and adding a free correcting photometric factor $(1 + b)$ in the fit.

As mentioned above, the amplitude of the shear-richness covariance term first depends on galaxy formation history in clusters, and second on the procedure used to populate halos in the simulation. As mentioned in Korytov et al. (2019), after defining the number of galaxies per halo, galaxy positions are drawn randomly in the halo environment (according to a generic NFW profile), thus not following the halo complex shape. This empha-

sizes that the cluster shear-richness correlation is also unrealistically lowered compared to real data. SkySim5000 (Abolfathi et al. 2021), the extension of cosmoDC2 to 5,000 deg^2 , has benefited from a better ray tracing resolution and a refined model of galaxy population in halos, based on the triaxial distribution of halo dark matter particles. This work can be extended with the SkySim5000 mock dataset, the latter having a higher degree of realism, to study shear-richness covariance at lower radii and with a larger cluster sample.

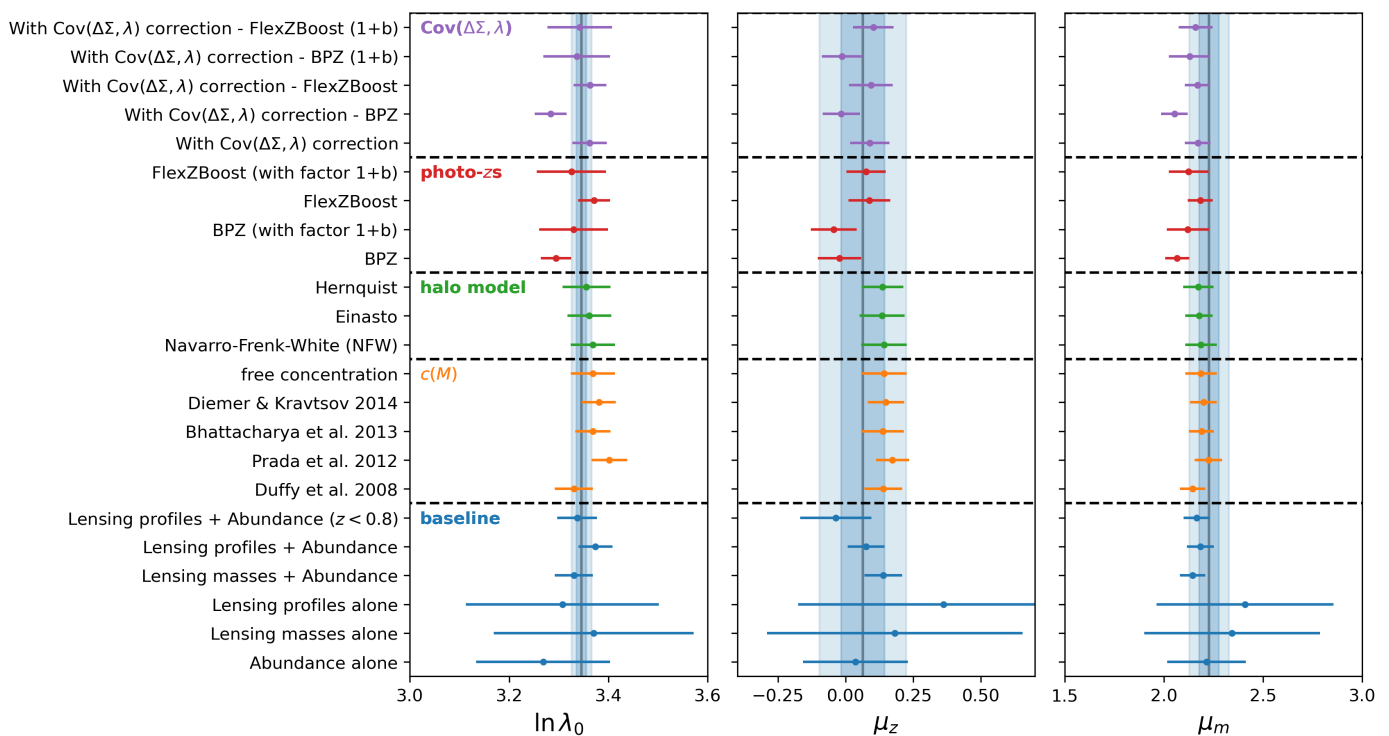


Fig. 13. Summary of the constraints on the scaling relation parameters (only $\ln \lambda_0$, μ_z and μ_m) obtained in Section 6. The vertical shaded region in each subplot represents the fiducial constraints presented in Section 4.4.1. For clarity, each color used for the plot corresponds to a subsection in Section 6.

Second, it depends on the cluster finder performance, which detects red-sequence galaxies. Since we have used the redMaPPer cluster catalog detected from mock datasets, the redMaPPer detection outcomes are rather idealistic compared with using real data.

These two effects explain somewhat the low amplitude (about 1 to 10%) of the shear-richness covariance²⁵.

6.4. Summary

We have conducted several analyses based on the lensing profiles and abundance of redMaPPer-detected clusters in the DC2 simulation, to constrain their mass-richness relation. We have defined a baseline analysis, with state-of-the-art modeling choices and estimators. From that, we have tested the impact of other modeling choices and observational systematics on the inferred mass-richness relation, also comparing it to a "fiducial" scaling relation. To do that, we have used a two-approach method, using either stacked lensing profiles or stacked lensing mass in combination with cluster count, to explore several analysis setups (fixing or not the cluster concentration, changing the dark matter density profile, adding shear-richness covariance).

In Figure 13, we display the constraints on the three parameters of the mean mass-richness relation in Eq. (2), namely $\ln \lambda_0$, μ_z and μ_m obtained in Section 6.1 (blue), in 6.2.1 (orange), in 6.2.2 (green), in 6.3.1 (red) and 6.3.2 (purple). The blue vertical bars correspond to the fiducial constraints listed in Table 1, with 1 and 2 σ confidence regions. We first conducted the analysis considering an ideal data setup, using true shapes of background sources (sheared versions of their true intrinsic ellipticities) and true redshifts. Despite the issue of the ray-tracing

²⁵ We also note that the $\ln(10)\beta_1/\mu_m$ factor in (38) is the order of unity, it does not change our conclusions.

resolution in the DC2 simulation impacting the innermost regions of cluster fields ($R < 1$ Mpc), we have found that the constraining the cluster scaling relation from a combination of cluster counts and lensing (either stacked masses or stacked profiles) provide tighter constraints than using each probe alone, due to their different degeneracies (see Figure 6). Using a Navarro-Frank-White (NFW, Navarro et al. (1997)) profile with the Duffy et al. (2008) concentration-mass relation and restricting the radial fitting range to the one-halo regime ($1 < R < 3.5$ Mpc) for the weak lensing analyses, the constraints are compatible with their "fiducial" values at the 1 σ level, the latter obtained from the match between redMaPPer-detected clusters and dark matter halos from the underlying N-body simulation of the DC2. This result allows us to validate our joint count and lensing approach, to address their reliability in constraining the cluster scaling relation. Moreover, we have conducted a series of robustness tests of the scaling relation parameters by varying the modeling choices of the stacked cluster weak lensing profiles. We have found that using an NFW profile in the one-halo regime, the choice of the concentration-mass relation has a low impact on the posteriors, always compatible at the 1 σ level with the free-concentration case. Similarly, varying the modeling of the cluster dark matter density by using different models for the dark matter density profile gives fairly robust constraints.

On the data side, we have tested the impact of photometric source redshifts on the parameter inference, by using the outputs of two photo- z codes ran on cosmoDC2 galaxy magnitudes, BPZ (Benítez 2011) and FlexZBoost (Izbicki & Lee 2017). From that, we have adapted the source selection to account for photo- z 's performances, and we have found that FlexZBoost leads to unbiased results compared to the true redshift case. Moreover, we found that the use of BPZ induces a $> 1\sigma$ bias on the normalization of the scaling relation, such bias that can be mitigated

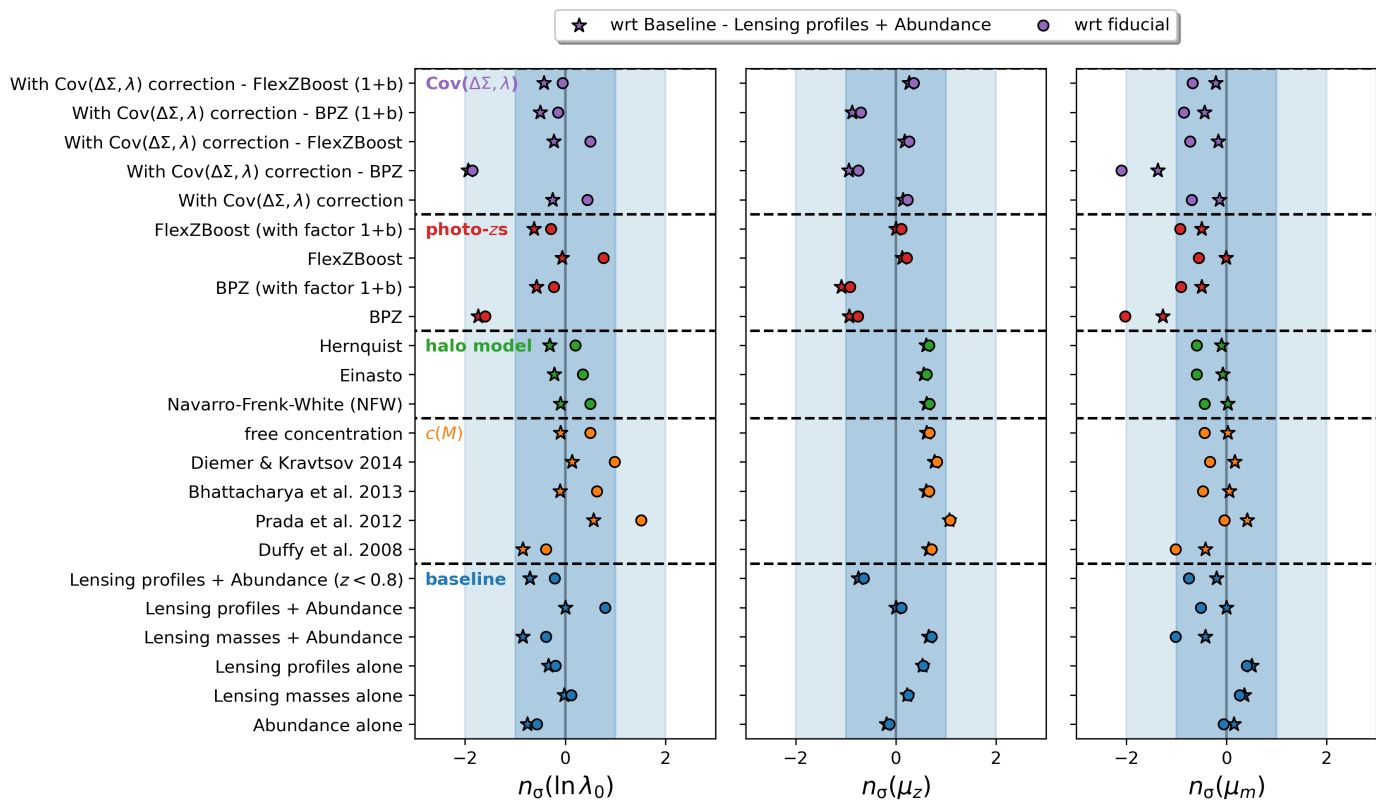


Fig. 14. Tension in numbers of σ between the different weak lensing/count analyses and the fiducial constraints (circle dots) for the parameters listed in Figure 13, and between the different analyses and the baseline weak lensing/count analysis (star dots).

using a correcting factor to be fitted jointly with the usual scaling relation parameters. We also found that in the considered fitting radial range of cluster lensing profiles, the impact of shear-richness covariance due to selection biases in the cluster-finding procedure is negligible.

We can complement the summary plot by measuring the *level of tension* of the different analyses with the fiducial constraints and the baseline analysis. We use the Gaussian tension metric (Raveri & Doux 2021; Leizerovich et al. 2024), that gives for a parameter x , the tension in numbers of σ between a Gaussian posterior \mathcal{P} and reference posterior \mathcal{P}_{fid} . It is given by

$$n_{\sigma}(x) = \frac{\langle x \rangle_{\mathcal{P}} - \langle x \rangle_{\mathcal{P}_{\text{fid}}}}{\sqrt{\sigma^2(x)_{\mathcal{P}} + \sigma^2(x)_{\mathcal{P}_{\text{fid}}}}} \quad (42)$$

where $\langle x \rangle_{\mathcal{P}}$ (resp. $\langle x \rangle_{\mathcal{P}_{\text{fid}}}$) is the mean of the parameter posterior $\mathcal{P}(x)$ (resp. $\mathcal{P}_{\text{fid}}(x)$) and $\sigma^2(x)_{\mathcal{P}}$ (resp. $\sigma^2(x)_{\mathcal{P}_{\text{fid}}}$) is the associated variance. For the different study cases, the level of tension with respect to the fiducial constraints (resp. the baseline - weak lensing profiles + count) is displayed in circle dots (resp. star dots) in Figure 14. This result enables us to accurately measure the Bayesian distance between various analysis setups and the fiducial constraints. We observe that combining probes (counts and lensing) does not significantly increase the tension while improving statistical precision. This demonstrates that our counts+lensing pipeline reliably describes the observables. Furthermore, regardless of the analysis choices made, the level of tension remains at most 2σ . This work also demonstrates that the baseline analysis is robust to variations in analysis setups, the latter shifting posteriors at most by 2σ .

7. Discussion and conclusion

To explore the full cosmological constraining power of galaxy clusters, a high precision on the cluster scaling relation must be reached. This can be done by using cluster count and cluster weak gravitational lensing as a joint probe to infer the cluster mass-richness relation and its intrinsic scatter in optical cluster cosmology. Cluster scaling relation constraints from lensing and counts constraints must be robust to any systematic effects, and in this paper, we have focused on cluster weak lensing-related ones.

In light of the first data from the Legacy Survey of Space and Time of the Vera Rubin Observatory, we investigate the mass-richness relation of redMaPPer-detected clusters with redshifts $0.2 < z < 1$ and richnesses $20 < \lambda < 200$ in the Dark Energy Science Collaboration Data Challenge 2 simulated dataset. We have inferred a 6-parameter log-normal cluster scaling relation, with mass and redshift dependence for both mean and variance, through the analysis of redMaPPer stacked lensing profiles that we supplemented with cluster count, to improve the constraining power. We have conducted a series of tests to investigate the variability of the mass-richness relation when changing the modeling of the cluster lensing profiles, as well as considering source photometric redshifts and shear-richness covariance. We have found that our constraints are rather stable when fitting the cluster lensing profiles within the one-halo regime ($1 < R < 3.5$ Mpc) when considering perfectly known source shapes, and true or photometric source redshifts. Moreover, we have shown that our results provide unbiased estimates of the fiducial redMaPPer cluster mass-richness relation. We are still far from the constraining power of LSST-like cluster sam-

ple statistics, $\sqrt{18,000/440} \approx 6.4$ times larger than what was reached in this work.

Moreover, the code work allows us to showcase the use of some of the software tools developed in the DESC in concrete cluster analysis and represents a step in the calibration, validation, and methodological development for a Y10-like LSST cluster survey. This work does a thorough rundown of all major systematics, except shape measurement, discussed hereafter. The framework used in this paper is well integrated into the CLMM and CCL pipelines and helps pave the way for the elaboration of cluster-based analyses in other official DESC pipeline codes such as TJPcov²⁶ (official DESC covariance calculator interface), Firecrown²⁷ (providing the DESC framework to implement likelihoods and sampling parameters), TXPipe²⁸ (DESC library for summary statistics measurement).

Due to the lack of ray-tracing resolution that motivated our conservative cut, we excluded the innermost regions, where the cluster lensing signal is the strongest. These scales are however crucial to enhance the precision of the weak lensing cluster masses. Analyzing such radial ranges requires particular attention to model the cluster lensing signal dilution by member galaxies (contamination, see e.g. Varga et al. (2019)) and mis-centering due to uncertainties on cluster finding methods (Zhang et al. 2019; Köhlinger et al. 2015) to be significant when referring to stacks of galaxy clusters.

Our analysis could benefit from further improvement to infer the redMaPPer cluster mass-richness relation; First, we have considered a fiducial Despali et al. (2015) halo mass function (HMF), but propagating calibration uncertainties of this relation in our pipeline could have a non-negligible impact (Artis et al. 2021; Kugel et al. 2024). Due to the noise level, we have neglected the off-diagonal terms in the covariances of the stacked lensing profiles. However, rather close radial bins are known to be somehow correlated due to the intrinsic variation of halo density profile and large scale structures (Wu et al. 2019) which could degrade the precision of our results, even being much smaller than the galaxy shot/shape noise contribution.

Moreover, for the stacked mass approach, the link between the "true" mean mass of a stack and the inferred mean weak lensing mass may be not trivial, contrary to what we used in Eq. (25), as a standard average mass over the redshift-richness cluster distribution. In reality, the excess surface density profile does not simply scale with the underlying cluster mass. For instance, Melchior et al. (2017) has proposed a simple model that the excess surface density follows $\Delta\Sigma(R|M) \propto M^{\Gamma(R|M)}$ where Γ is the logarithmic slope of the excess surface density²⁹, such that the stacked weak lensing mass $\langle \widehat{M}_{\text{WL}}^{\text{stack}} \rangle$ has to be modeled by $\sim \langle m^{\Gamma} \rangle^{1/\Gamma}$. Such non-linear dependence can be accounted for in the stacked mass modeling in Eq. (25). Beyond this rather simple correction to link the stacked lensing mass to the true average mass of the stack, McClintock et al. (2019) have used simulations to reconstruct the stack lensing signal around clusters with masses drawn from known $P(M|\lambda)$ relation, as well as concentrations, miscentering offsets drawn from specific distributions. They found that the bias between the true average mass and stacked weak lensing mass may reach 10% (see their Figure 9) and has a strong richness and redshift dependence, denoting

a strong impact of intrinsic scatter (in richness, concentration, mis-centering, etc).

Even if not sensitive to mis-centering in our analysis (due to our restrictive low radial cut), we have considered a *fixed* concentration-mass relation, however, it is known that cluster concentrations are scattered around a mean $c(M)$ relation (see e.g. Bullock et al. (2001); Darragh-Ford et al. (2023)). This effect is particularly important in stacked analysis especially at small radii, accounting for this effect should degrade the precision of our obtained constraints by lowering the sensitivity of our model.

Finally, noise in galaxy shapes is one of the current main sources of scatter in weak lensing cluster mass estimation. First, as already introduced, it originates from the intrinsic scatter of galaxy shapes, which is more and more mitigated by the increasing statistics of ongoing and future optical surveys. Second, it originates from the galaxy shape measurement algorithms, returning dispersed and biased estimations of intrinsic galaxy ellipticities. Shape reconstruction methods generally need to be calibrated from simulation or internally. Dispersed measured shapes as well as calibration uncertainties in these algorithms inevitably propagate to the cluster mass estimates, downgrading their precision. For that, the DC2 object catalog (Abolfathi et al. 2021) was built using the Rubin LSST science pipeline, by identifying galaxies on cosmoDC2-based realistic images of the sky, including several realistic observational effects, such as atmospheric turbulence, telescope optics, and some detector effects. Several codes are used to measure shapes of detected galaxies, such as HSM (Hirata & Seljak 2003; Mandelbaum et al. 2005) used on the HSC data (Mandelbaum et al. 2018), and METACALIBRATION (Sheldon & Huff 2017), used in the DES-Y3 cosmic shear analysis in Abbott et al. (2022). Ongoing efforts in DESC aim at studying the impact of galaxy detection and shape measurement in cluster fields, on the accuracy and the precision of cluster mass estimates (Ramel et al. in prep), which are essential to handle the full error budget on the mass-richness relation, in preparation for LSST cluster cosmology.

Acknowledgments

This paper has undergone internal review by the LSST Dark Energy Science Collaboration. The authors thank the internal reviewers Tomomi Sunayama and Shenming Fu for their valuable comments. The authors thank Fabien Lacasa for useful discussions and for their help in using the PySSC code. The authors thank Dominique Boutigny for his help in using Qserv to access the cosmoDC2 simulated datasets at CC-IN2P3.

CP conceptualized the project, developed the code, led the analysis, contributed to the paper's structure and text, and oversaw the overall writing process. ZZ contributed to the shear-richness covariance analysis, the early development of the analysis framework and code, and the paper's structure and text. MA developed the DESC matching library CIEvaR and contributed to the paper's structure and text. CC assisted with project conceptualization and advising, participated in the early development and review of the analysis framework and code, and contributed to the paper's structure and text. TG provided the parametrization of the redMaPPer selection function. MR prepared the matched cosmoDC2-redMaPPer catalog, reviewed various aspects of the analysis, and contributed to the paper's structure and text. The remaining authors generated the data used in this work, contributed to the project's infrastructure, and participated in discussions interpreting the results.

The DESC acknowledges ongoing support from the Institut National de Physique Nucléaire et de Physique des Par-

²⁶ <https://github.com/LSSTDESC/tjpcov>

²⁷ <https://github.com/LSSTDESC/firecrown>

²⁸ <https://github.com/LSSTDESC/txpipe>

²⁹ Melchior et al. (2017), found typical value of $\Gamma = 0.74$ for an NFW profile.

ticules in France; the Science & Technology Facilities Council in the United Kingdom; and the Department of Energy, the National Science Foundation, and the LSST Corporation in the United States. DESC uses resources of the IN2P3 Computing Center (CC-IN2P3–Lyon/Villeurbanne - France) funded by the Centre National de la Recherche Scientifique; the National Energy Research Scientific Computing Center, a DOE Office of Science User Facility supported by the Office of Science of the U.S. Department of Energy under Contract No. DE-AC02-05CH11231; STFC DiRAC HPC Facilities, funded by UK BIS National E-infrastructure capital grants; and the UK particle physics grid, supported by the GridPP Collaboration. This work was performed in part under DOE Contract DE-AC02-76SF00515. MA is supported by the PRIN 2022 project EMC2 - Euclid Mission Cluster Cosmology: unlock the full cosmological utility of the Euclid photometric cluster catalog (code no. J53D23001620006). CA acknowledges support from DOE grant DE-SC0019193 and the Leinweber Center for Theoretical Physics. AF acknowledges support from the National Science Foundation under Cooperative Agreement 2421782 and the Simons Foundation award MPS-AI-00010515.

We thank the developers and maintainers of the following softwares used in this work: NumPy (van der Walt et al. 2011), SciPy (Jones et al. 2001), Matplotlib (Hunter 2007), GetDist (Lewis 2019), emcee (Foreman-Mackey et al. 2013), Astropy (Astropy Collaboration et al. 2013), Jupyter (Kluyver et al. 2016).

References

- Abbott, T., Aguena, M., Alarcon, A., et al. 2020, *Phys. Rev. D*, 102, 023509
- Abbott, T., Aguena, M., Alarcon, A., et al. 2022, *Phys. Rev. D*, 105, 023520
- Abdullah, M. H., Klypin, A., & Wilson, G. 2020, *ApJ*, 901, 90
- Abell, P. A., Allison, J., Anderson, S. F., et al. 2009, arXiv e-prints, arXiv:0912.0201
- Abolfathi, B., Alonso, D., Armstrong, R., et al. 2021, *ApJS*, 253, 31
- Ade, P., Aghanim, N., Armitage-Caplan, C., et al. 2014, *A&A*, 571, A20
- Ade, P., Aghanim, N., Armitage-Caplan, C., et al. 2016, *A&A*, 594, A24
- Aguena, M., Alves, O., Annis, J., et al. 2023, arXiv e-prints, arXiv:2309.06593
- Aguena, M., Avestruz, C., Combet, C., et al. 2021, *MNRAS*, 508, 6092
- Aguena, M., Benoist, C., da Costa, L. N., et al. 2021, *MNRAS*, 502, 4435
- Aguena, M. & Lima, M. 2018, *Phys. Rev. D*, 98, 123529
- Aihara, H., Armstrong, R., Bickerton, S., et al. 2018, *PASJ*, 70, S8
- Allen, S. W., Evrard, A. E., & Mantz, A. B. 2011, *ARA&A*, 49, 409
- Anbajagane, D., Evrard, A. E., Farahi, A., et al. 2020, *MNRAS*, 495, 686
- Artis, E., Melin, J.-B., Bartlett, J. G., & Murray, C. 2021, *A&A*, 649, A47
- Astropy Collaboration, Robitaille, T. P., Tollerud, E. J., et al. 2013, *A&A*, 558, A33
- Bartlett, J. G. 1997, 126, 365
- Baxter, E. J., Rozo, E., Jain, B., Rykoff, E., & Wechsler, R. H. 2016, *MNRAS*, 463, 205
- Becker, M. R. & Kravtsov, A. V. 2011, *ApJ*, 740, 25
- Bellagamba, F., Roncarelli, M., Maturi, M., & Moscardini, L. 2018, *MNRAS*, 473, 5221
- Benítez, N. 2011, *ASCL*, ascl:1108.011
- Benson, A. J. 2012, *New A*, 17, 175
- Bernstein, G. M. & Nakajima, R. 2009, *ApJ*, 693, 1508
- Bhattacharya, S., Habib, S., Heitmann, K., & Vikhlinin, A. 2013, *ApJ*, 766, 32
- Binggeli, B. 1982, *A&A*, 107, 338
- Bocquet, S., Grandis, S., Bleem, L. E., et al. 2023, arXiv e-prints, arXiv:2310.12213
- Bocquet, S., Grandis, S., Bleem, L. E., et al. 2024, arXiv e-prints, arXiv:2401.02075
- Bulbul, E., Liu, A., Kluge, M., et al. 2024, *A&A*, 685, A106
- Bullock, J. S., Kolatt, T. S., Sigad, Y., et al. 2001, *MNRAS*, 321, 559
- Buote, D. A. & Lewis, A. D. 2004, *ApJ*, 604, 116
- Chang, C., Jarvis, M., Jain, B., et al. 2013, *MNRAS*, 434, 2121–2135
- Chen, K.-F., Chiu, I.-N., Oguri, M., et al. 2024, arXiv e-prints, arXiv:2406.11966
- Chisari, N. E., Alonso, D., Krause, E., et al. 2019, *ApJS*, 242, 2
- Chiu, I.-N., Chen, K.-F., Oguri, M., et al. 2024, arXiv e-prints, arXiv:2406.11970
- Corless, V. L. & King, L. J. 2009, *MNRAS*, 396, 315
- Costanzi, M., Rozo, E., Rykoff, E. S., et al. 2018, *MNRAS*, 482, 490–505
- Costanzi, M., Rozo, E., Simet, M., et al. 2019, *MNRAS*, 488, 4779
- Cromer, D., Battaglia, N., Miyatake, H., & Simet, M. 2022, *J. Cosmology Astropart. Phys.*, 2022, 034
- Darragh-Ford, E., Mantz, A. B., Rasia, E., et al. 2023, *MNRAS*, 521, 790
- Despali, G., Giocoli, C., Angulo, R. E., et al. 2015, *MNRAS*, 456, 2486
- Despali, G., Giocoli, C., & Tormen, G. 2014, *MNRAS*, 443, 3208
- Diemer, B. 2023, *MNRAS*, 519, 3292
- Diemer, B. & Joyce, M. 2019, *ApJ*, 871, 168
- Diemer, B. & Kravtsov, A. V. 2014, *ApJ*, 789, 1
- Duffy, A. R., Schaye, J., Kay, S. T., & Dalla Vecchia, C. 2008, *MNRAS*, 390, L64
- Einasto, J. 1965, *Trudy Astrofizicheskogo Instituta Alma-Ata*, 5, 87
- Escoffier, S., Cousinou, M. C., Tilquin, A., et al. 2016, arXiv e-prints, arXiv:1606.00233
- Euclid Collaboration, Adam, R., Vannier, M., et al. 2019, *A&A*, 627, A23
- Evrard, A. E., Arnault, P., Huterer, D., & Farahi, A. 2014, *MNRAS*, 441, 3562
- Farahi, A., Anbajagane, D., & Evrard, A. E. 2022, *ApJ*, 931, 166
- Farahi, A., Evrard, A. E., McCarthy, I., Barnes, D. J., & Kay, S. T. 2018, *MNRAS*, 478, 2618
- Farahi, A., Evrard, A. E., Rozo, E., Rykoff, E. S., & Wechsler, R. H. 2016, *MNRAS*, 460, 3900
- Foreman-Mackey, D., Hogg, D. W., Lang, D., & Goodman, J. 2013, *PASP*, 125, 306
- Fumagalli, A., Costanzi, M., Saro, A., Castro, T., & Borgani, S. 2023, arXiv e-prints, arXiv:2310.09146
- Fumagalli, A., Saro, A., Borgani, S., et al. 2021, *A&A*, 652, A21
- Gao, L., Navarro, J. F., Cole, S., et al. 2008, *MNRAS*, 387, 536
- Ghirardini, V., Bulbul, E., Artis, E., et al. 2024, arXiv e-prints, arXiv:2402.08458
- Giocoli, C., Marulli, F., Moscardini, L., et al. 2021, *A&A*, 653, A19
- Gouyou Beauchamps, S., Lacasa, F., Tutusaus, I., et al. 2022, *A&A*, 659, A128
- Graham, M. L., Connolly, A. J., Ivezić, Z., et al. 2017, *The Astronomical Journal*, 155, 1
- Grandis, S., Bocquet, S., Mohr, J. J., Klein, M., & Dolag, K. 2021, *MNRAS*, 507, 5671
- Grandis, S., Ghirardini, V., Bocquet, S., et al. 2024, *A&A*, 687, A178
- Grishin, K., Mei, S., & Ilić, S. 2023, *A&A*, 677, A101
- Gruen, D., Seitz, S., Becker, M. R., Friedrich, O., & Mana, A. 2015, *MNRAS*, 449, 4264
- Hasselfield, M., Hilton, M., Marriage, T. A., et al. 2013, *J. Cosmology Astropart. Phys.*, 2013, 008
- Hearin, A., Korytov, D., Kovacs, E., et al. 2020, *MNRAS*, 495, 5040
- Heitmann, K., Finkel, H., Pope, A., et al. 2019, *ApJS*, 245, 16
- Hernández-Martín, B., Schrabback, T., Hoekstra, H., et al. 2020, *A&A*, 640, A117
- Hetterscheidt, M., Erben, T., Schneider, P., et al. 2005, *A&A*, 442, 43
- Hirata, C. & Seljak, U. 2003, *MNRAS*, 343, 459
- Hoekstra, H. 2003, *MNRAS*, 339, 1155
- Hogg, D. W. 1999, arXiv e-prints, astro
- Hu, W. & Kravtsov, A. V. 2003, *ApJ*, 584, 702–715
- Hunter, J. D. 2007, *Computing in Science and Engineering*, 9, 90
- Izbicki, R. & Lee, A. B. 2017, arXiv e-prints, arXiv:1704.08095
- James, F. & Roos, M. 1975, *Comput. Phys. Commun.*, 10, 343
- Jimeno, P., Diego, J. M., Broadhurst, T., De Martino, I., & Lazkoz, R. 2018, *MNRAS*, 478, 638
- Jing, Y. P. & Suto, Y. 2002, *ApJ*, 574, 538
- Johnston, D. E., Sheldon, E. S., Wechsler, R. H., et al. 2007, arXiv e-prints, arXiv:0709.1159
- Jones, E., Oliphant, T., & Peterson, P. 2001
- Kaiser, N. 1984, *ApJ*, 284, L9
- Kluyver, T., Ragan-Kelley, B., Pérez, F., et al. 2016, in *IOS Press*, 87–90
- Klypin, A., Yepes, G., Gottlöber, S., Prada, F., & Heß, S. 2016, *MNRAS*, 457, 4340
- Köhlinger, F., Hoekstra, H., & Eriksen, M. 2015, *MNRAS*, 453, 3107
- Komatsu, E., Dunkley, J., Nolta, M. R., et al. 2009, *ApJS*, 180, 330
- Komatsu, E., Smith, K. M., Dunkley, J., et al. 2011, *ApJS*, 192, 18
- Korytov, D., Hearin, A., Kovacs, E., et al. 2019, *ApJS*, 245, 26
- Kovacs, E., Mao, Y.-Y., Aguena, M., et al. 2022, *OJAp*, 5, 1
- Kravtsov, A. V. & Borgani, S. 2012, *ARA&A*, 50, 353
- Kugel, R., Schaye, J., Schaller, M., Forouhar Moreno, V. J., & McGibbon, R. J. 2024, arXiv e-prints, arXiv:2408.17217
- Lacasa, F., Lima, M., & Aguena, M. 2018, *A&A*, 611, A83
- Laureijs, R., Amiaux, J., Arduini, S., et al. 2011, arXiv e-prints, arXiv:1110.3193
- Lee, A., Wu, H.-Y., Salcedo, A. N., et al. 2024
- Lee, B. E., Le Brun, A. M. C., Haq, M. E., et al. 2018, *MNRAS*, 479, 890
- Leizerovich, M., Landau, S. J., & Scóccola, C. G. 2024, *Physics Letters B*, 855, 138844
- Lesci, G. F., Marulli, F., Moscardini, L., et al. 2022, *A&A*, 659, A88
- Lewis, A. 2019, arXiv e-prints, arXiv:1910.13970
- LSST Dark Energy Science Collaboration. 2012, arXiv e-prints, arXiv:1211.0310

- Mandelbaum, R., Hirata, C. M., Seljak, U., et al. 2005, *MNRAS*, 361, 1287
- Mandelbaum, R., Lanusse, F., Leauthaud, A., et al. 2018, *MNRAS*, 481, 3170
- Mantz, A., Allen, S. W., Ebeling, H., & Rapetti, D. 2008, *MNRAS*, 387, 1179
- Mantz, A. B. 2019, *MNRAS*, 485, 4863
- Mantz, A. B., von der Linden, A., Allen, S. W., et al. 2015, *MNRAS*, 446, 2205
- McClintock, T., Varga, T. N., Gruen, D., et al. 2019, *MNRAS*, 482, 1352
- Melchior, P., Gruen, D., McClintock, T., et al. 2017, *MNRAS*, 469, 4899–4920
- Mistele, T. & Durakovic, A. 2024, arXiv e-prints, arXiv:2408.07026
- Mulroy, S. L., Farahi, A., Evrard, A. E., et al. 2019, *MNRAS*, 484, 60
- Murata, R., Oguri, M., Nishimichi, T., et al. 2019, *PASJ*, 71, 107
- Murray, C., Bartlett, J. G., Artis, E., & Melin, J.-B. 2022, *MNRAS*, 512, 4785
- Navarro, J. F., Frenk, C. S., & White, S. D. M. 1997, *ApJ*, 490, 493
- Nord, B., Stanek, R., Rasia, E., & Evrard, A. E. 2008, *MNRAS*, 383, L10
- Oguri, M., Lee, J., & Suto, Y. 2003, *ApJ*, 599, 7
- Oguri, M. & Takada, M. 2011, *Phys. Rev. D*, 83
- Oguri, M., Takada, M., Okabe, N., & Smith, G. P. 2010, *MNRAS*
- Pacaud, F., Pierre, M., Melin, J.-B., et al. 2018, *A&A*, 620, A10
- Park, Y., Sunayama, T., Takada, M., et al. 2023, *MNRAS*, 518, 5171
- Parroni, C., Mei, S., Erben, T., et al. 2017, *ApJ*, 848, 114
- Payerne, C., Murray, C., Combet, C., et al. 2023, *MNRAS*, 520, 6223
- Payerne, C., Murray, C., Combet, C., & Penna-Lima, M. 2024, *MNRAS*, 532, 381
- Penna-Lima, M., Makler, M., & Wuensche, C. 2014, *J. Cosmology Astropart. Phys.*, 2014, 039–039
- Phriksee, A., Jullo, E., Limousin, M., et al. 2020, *MNRAS*, 491, 1643
- Planck Collaboration, Ade, P. A. R., Aghanim, N., et al. 2016, *A&A*, 594, A27
- Poisson, S. D. 1837, Bachelier, Imprimeur-Librairie
- Prada, F., Klypin, A. A., Cuesta, A. J., Betancort-Rijo, J. E., & Primack, J. 2012, *MNRAS*, 423, 3018
- Pratt, G. W., Arnaud, M., Biviano, A., et al. 2019, *Space Sci. Rev.*, 215, 25
- Raveri, M. & Doux, C. 2021, *Phys. Rev. D*, 104, 043504
- Rozo, E., Evrard, A. E., Rykoff, E. S., & Bartlett, J. G. 2014, *MNRAS*, 438, 62
- Rykoff, E. S., Rozo, E., Busha, M. T., et al. 2014, *ApJ*, 785, 104
- Rykoff, E. S., Rozo, E., Hollowood, D., et al. 2016, *ApJS*, 224, 1
- Sadibekova, T., Pierre, M., Clerc, N., et al. 2014, *A&A*, 571, A87
- Sanderson, A. J. R. & Ponman, T. J. 2009, *MNRAS*, 402, 65
- Saro, A., Bocquet, S., Rozo, E., et al. 2015, *MNRAS*, 454, 2305
- Schmidt, S. J., Malz, A. I., Soo, J. Y. H., et al. 2020, *MNRAS*, 499, 1587
- Schneider, M. D., Frenk, C. S., & Cole, S. 2012, *J. Cosmology Astropart. Phys.*, 2012, 030
- Schneider, P., Ehlers, J., & Falco, E. E. 1992, *Gravitational Lenses*
- Sereno, M., Fedeli, C., & Moscardini, L. 2016, *J. Cosmology Astropart. Phys.*, 2016, 042
- Sheldon, E. S. & Huff, E. M. 2017, *ApJ*, 841, 24
- Sheldon, E. S., Johnston, D. E., Frieman, J. A., et al. 2004, *AJ*, 127, 2544
- Sheth, R. K., Mo, H. J., & Tormen, G. 2001, *MNRAS*, 323, 1
- Shirasaki, M. & Takada, M. 2018, *MNRAS*, 478, 4277
- Simet, M., McClintock, T., Mandelbaum, R., et al. 2017, *MNRAS*, 466, 3103
- Sommer, M. W., Schrabback, T., Applegate, D. E., et al. 2022, *MNRAS*, 509, 1127
- Spergel, D., Gehrels, N., Baltay, C., et al. 2015, arXiv e-prints, arXiv:1503.03757
- Sunayama, T., Miyatake, H., Sugiyama, S., et al. 2023, arXiv e-prints, arXiv:2309.13025
- Sunayama, T., Park, Y., Takada, M., et al. 2020, *MNRAS*, 496, 4468–4487
- Tinker, J. L., Robertson, B. E., Kravtsov, A. V., et al. 2010, *ApJ*, 724, 878
- Umetsu, K. 2020, *A&A Rev.*, 28
- van der Walt, S., Colbert, S. C., & Varoquaux, G. 2011, *Computing in Science and Engineering*, 13, 22
- Varga, T. N., DeRose, J., Gruen, D., et al. 2019, *MNRAS*, 489, 2511
- Vogt, S. M. L., Bocquet, S., Davies, C. T., et al. 2024, arXiv e-prints, arXiv:2409.13556
- Wang, J., Bose, S., Frenk, C. S., et al. 2020, *Nature*, 585, 39
- Wright, A. H., Hildebrandt, H., van den Busch, J. L., & Heymans, C. 2020, *A&A*, 637, A100
- Wu, H.-Y., Costanzi, M., To, C.-H., et al. 2022, *MNRAS*, 515, 4471
- Wu, H.-Y., Weinberg, D. H., Salcedo, A. N., Wibking, B. D., & Zu, Y. 2019, *MNRAS*, 490, 2606
- Zhang, Y., Jeltama, T., Hollowood, D. L., et al. 2019, *MNRAS*, 487, 2578
- Zhang, Z., Farahi, A., Nagai, D., et al. 2024, *MNRAS*[arXiv:2310.18266]
- Zhang, Z., Wu, H.-Y., Zhang, Y., et al. 2023, *MNRAS*, 523, 1994–2013
- Zwicky, F. 1937, *ApJ*, 86, 217

Appendix A: Constraints of the scaling relation: summary table

We list in Table A.1 the values of the scaling relation parameters obtained from cluster count and/or cluster lensing in Section 6.1 (baseline analysis), Section 6.2.1 (impact of $c(M)$ relation), Section 6.2.2 (impact of density profile) Section 6.3.1 (impact of source galaxy photometric redshifts) and Section 6.3.2 (impact of shear-richness covariance).

Appendix B: Stability of the fiducial cluster scaling relation

The fiducial scaling relation used throughout this paper was derived from the matched catalog between redMaPPer clusters and cosmoDC2 halos (covering $\lambda > 5$ and $M_{200c} > 10^{13} M_{\odot}$). In this appendix, we discuss the various cuts applied to the matched catalog prior to inferring the fiducial relation using the likelihood in Eq. (30). The parameter posteriors (showing only the mean scaling relation parameters for simplicity) derived using the *full* matched catalog are shown as green unfilled contours in Figure B.1 (left panel).

Initially, we assume the matched catalog is unaffected by the purity of the redMaPPer cluster finder (since *false* detections have been removed). However, completeness still impacts the matched catalog, since not all halos, particularly at low mass, are detected by the redMaPPer cluster finder. Thus, the likelihood in Eq. (30) should ideally account for *missing* halos. To mitigate this issue, we impose a low mass cut of $M_{200c} > 4 \times 10^{13} M_{\odot}$, ensuring redMaPPer completeness is at least 50%. The corrected posterior is displayed as magenta unfilled contours in Figure B.1 (left panel).

Additionally, our cluster scaling relation model in Eq. (1) does not account for Poisson noise in redMaPPer richness determination. This noise can be incorporated by revising Eq. (1) as

$$P(\lambda|m, z) = \int_0^{+\infty} \mathcal{P}(\lambda|\lambda_{\text{int}}) P(\lambda_{\text{int}}|m, z) d\lambda_{\text{int}} \quad (\text{B.1})$$

where $\mathcal{P}(\lambda|\lambda_{\text{int}})$ is the Poisson distribution and $P(\lambda_{\text{int}}|m, z)$ represents the probability density function for the *intrinsic* richness, which can be expressed with the same equation as in Eq. (1), but with intrinsic variance only. This updated $P(\lambda|m, z)$ above can be approximated by using the same $P(\lambda_{\text{int}}|m, z)$ while updating the variance

$$\sigma_{\ln \lambda|m, z}^2 \approx [\sigma_{\ln \lambda|m, z}]_{\text{int}}^2 + \frac{\exp(\langle \ln \lambda|m, z \rangle) - 1}{\exp(2\langle \ln \lambda|m, z \rangle)} \quad (\text{B.2})$$

where $[\sigma_{\ln \lambda|m, z}]_{\text{int}}^2$ is provided in Eq. (3), now only describing the intrinsic variance of richness. The impact of the Poisson noise, represented by the second term (see e.g. Zhang et al. (2023)), diminishes for large richness. Consequently, we apply a low richness cut $\lambda > 10$ to align with the Poisson-free distribution in Eq. (1).

Combining this with the mass cut $M_{200c} > 4 \times 10^{13} M_{\odot}$, the constraints are represented as black dashed unfilled contours in Figure B.1 (left panel) and are identified as our *fiducial* choice. We observe that the three fiducial constraints agree within $< 2\sigma$ of the baseline count+weak lensing posteriors (filled contours). We also explore a stricter cut, $\lambda > 20$, combined with $M_{200c} > 4 \times 10^{13} M_{\odot}$ (cyan contours). This $\lambda > 20$ scenario results in

larger error bars (still compatible with count+weak lensing constraints) but biases the mass slope μ_m lower than other choices. In fact, from 1 (left), the $\lambda > 20$ cut overemphasizes high-richness clusters in the fiducial fit, even after correcting the distribution $P(\lambda|m, z)$ using a truncated Gaussian to account for the minimum richness. While we adopt the black dashed contours as our fiducial constraints, further investigations are warranted.

Appendix C: Impact of the radial fitting range on the scaling relation parameters

In this appendix, we test the impact of the fitting radial range $[1, R_{\text{max}}]$ of the stacked excess surface density profiles on the scaling relation parameters. Our baseline adopts a conservative choice of $R_{\text{max}} = 3.5$ Mpc for fitting the stacked excess surface density profiles, ensuring sensitivity to the one-halo regime only. At larger radii, the influence of the two-halo term is expected to become more significant, and modeling the stacked profiles using only the one-halo regime may be insufficient.

We repeat the scaling relation parameter fit using $R_{\text{max}} = 5.5$ and $R_{\text{max}} = 10$ Mpc, respectively. The mean scaling relation parameters for these different fitting radial ranges are shown in Figure B.1 (right panel). Both new cuts yield conclusions consistent with the baseline, with shifts of less than $< 1\sigma$ compared to the baseline constraints.

Interestingly, the results for $R_{\text{max}} = 10$ Mpc are close to the baseline constraints, despite the absence of modeling for the two-halo term in the stacked lensing profile. We attribute this to the lower signal-to-noise ratio (SNR) of measurements at large scales, reducing the impact of the two-halo term. However, with larger datasets, the two-halo term must be accurately modeled beyond $R = 4$ Mpc (Murata et al. 2019; McClintock et al. 2019; Melchior et al. 2017).

Appendix D: Derivation of the selection bias

In this appendix, we use the notation

$$N(m, z) = \frac{dn(m, z)}{dm} \frac{d^2V(z)}{dzd\Omega}. \quad (\text{D.1})$$

We can consider that the measured shear and richness are correlated, such as that can be modeled as correlated random variables via $P(\Delta\Sigma, \lambda|m)$. Then, the average excess surface density profile within the i -th redshift bin and the j -th richness bin is given by

$$\langle \Delta\Sigma \rangle \propto \int_{z_i}^{z_{i+1}} dz \int_{m_{\text{min}}}^{m_{\text{max}}} dm N(m, z) \int_{\lambda_j}^{\lambda_{j+1}} d\lambda P(\lambda|m, z) \langle \Delta\Sigma|m, \lambda, z \rangle, \quad (\text{D.2})$$

From Wu et al. (2022), we consider $P(\Delta\Sigma, \lambda|m)$ as a multi-variate Gaussian distribution, with means $\langle \Delta\Sigma|m, z \rangle$ and $\langle \ln \lambda|m, z \rangle$ and with covariance matrix

$$C = \begin{pmatrix} \sigma_{\ln \lambda}^2 & r\sigma_{\ln \lambda}\sigma_{\Delta\Sigma} \\ r\sigma_{\ln \lambda}\sigma_{\Delta\Sigma} & \sigma_{\Delta\Sigma}^2 \end{pmatrix}. \quad (\text{D.3})$$

From Wu et al. (2019) (see their Eq. 8), the conditional mean of $\Delta\Sigma$ is given by

$$\langle \Delta\Sigma|m, \lambda, z \rangle = \langle \Delta\Sigma|m, z \rangle + r \frac{\sigma_{\Delta\Sigma}}{\sigma_{\ln \lambda}} [\ln \lambda - \langle \ln \lambda|m, z \rangle]. \quad (\text{D.4})$$

From Farahi et al. (2022), we can approximate the halo mass function to the form

$$N(m, z) \approx A(z) \exp[-\beta_1 \ln m]. \quad (\text{D.5})$$

Parameters	$\ln \lambda_0$	μ_z	μ_m	$\sigma_{\ln \lambda_0}$	σ_z	σ_m
Baseline analysis, Section 6.1						
Abundance alone	3.27 ± 0.14	0.04 ± 0.19	2.22 ± 0.20	0.53 ± 0.11	0.06 ± 0.25	-0.11 ± 0.14
Lensing masses alone	3.37 ± 0.20	0.18 ± 0.47	2.34 ± 0.44	0.52 ± 0.10	-0.03 ± 0.32	-0.00 ± 0.15
Lensing profiles alone	3.31 ± 0.19	0.36 ± 0.54	2.41 ± 0.45	0.54 ± 0.08	-0.05 ± 0.33	-0.03 ± 0.15
Lensing masses + Abundance	3.33 ± 0.04	0.14 ± 0.07	2.14 ± 0.06	0.58 ± 0.02	0.06 ± 0.11	0.13 ± 0.07
Lensing profiles + Abundance	3.37 ± 0.03	0.08 ± 0.07	2.18 ± 0.07	0.53 ± 0.03	0.20 ± 0.11	0.14 ± 0.05
Lensing profiles + Abundance ($z < 0.8$)	3.34 ± 0.04	-0.04 ± 0.13	2.16 ± 0.07	0.54 ± 0.02	0.17 ± 0.15	0.08 ± 0.08
Impact of the concentration-mass relation, Section 6.2.1						
Duffy et al. 2008	3.33 ± 0.04	0.14 ± 0.07	2.14 ± 0.06	0.58 ± 0.02	0.06 ± 0.11	0.13 ± 0.07
Prada et al. 2012	3.40 ± 0.04	0.17 ± 0.06	2.22 ± 0.07	0.52 ± 0.03	0.02 ± 0.10	0.16 ± 0.05
Bhattacharya et al. 2013	3.37 ± 0.04	0.14 ± 0.08	2.19 ± 0.06	0.55 ± 0.03	0.07 ± 0.12	0.14 ± 0.05
Diemer Kravtsov 2014	3.38 ± 0.03	0.15 ± 0.07	2.20 ± 0.07	0.54 ± 0.03	0.06 ± 0.12	0.15 ± 0.05
free concentration	3.37 ± 0.04	0.14 ± 0.08	2.19 ± 0.08	0.54 ± 0.03	0.08 ± 0.14	0.15 ± 0.06
Impact of the dark matter density profile, Section 6.2.2						
Navarro-Frenk-White (NFW)	3.37 ± 0.04	0.14 ± 0.08	2.19 ± 0.08	0.54 ± 0.03	0.08 ± 0.14	0.15 ± 0.06
Einasto	3.36 ± 0.04	0.13 ± 0.08	2.18 ± 0.07	0.55 ± 0.03	0.08 ± 0.14	0.14 ± 0.06
Hernquist	3.36 ± 0.05	0.14 ± 0.08	2.17 ± 0.08	0.55 ± 0.03	0.08 ± 0.13	0.13 ± 0.06
Impact of source photometric redshifts, Section 6.3.1						
true source redshifts	3.37 ± 0.03	0.08 ± 0.07	2.18 ± 0.07	0.53 ± 0.03	0.20 ± 0.11	0.14 ± 0.05
BPZ	3.29 ± 0.03	-0.02 ± 0.08	2.07 ± 0.06	0.59 ± 0.02	0.32 ± 0.11	0.14 ± 0.06
BPZ (with factor 1+b)	3.33 ± 0.07	-0.04 ± 0.09	2.12 ± 0.11	0.55 ± 0.06	0.40 ± 0.15	0.13 ± 0.06
FlexZBoost	3.37 ± 0.03	0.09 ± 0.08	2.18 ± 0.06	0.54 ± 0.02	0.17 ± 0.12	0.14 ± 0.05
FlexZBoost (with factor 1+b)	3.33 ± 0.07	0.08 ± 0.07	2.12 ± 0.10	0.57 ± 0.06	0.17 ± 0.13	0.14 ± 0.06
Impact of source photometric redshifts, Section 6.3.2						
Without Cov($\Delta\Sigma, \lambda$) correction	3.37 ± 0.03	0.08 ± 0.07	2.18 ± 0.07	0.53 ± 0.03	0.20 ± 0.12	0.14 ± 0.04
With Cov($\Delta\Sigma, \lambda$) correction	3.36 ± 0.03	0.09 ± 0.07	2.17 ± 0.06	0.54 ± 0.02	0.17 ± 0.12	0.14 ± 0.05
With Cov($\Delta\Sigma, \lambda$) correction - BPZ	3.28 ± 0.03	-0.02 ± 0.07	2.05 ± 0.07	0.61 ± 0.02	0.30 ± 0.10	0.14 ± 0.06
With Cov($\Delta\Sigma, \lambda$) correction - FlexZBoost	3.36 ± 0.03	0.09 ± 0.08	2.17 ± 0.06	0.55 ± 0.02	0.16 ± 0.13	0.15 ± 0.05
With Cov($\Delta\Sigma, \lambda$) correction - BPZ (1+b)	3.34 ± 0.07	-0.01 ± 0.08	2.13 ± 0.10	0.55 ± 0.06	0.36 ± 0.14	0.14 ± 0.06
With Cov($\Delta\Sigma, \lambda$) correction - FlexZBoost (1+b)	3.34 ± 0.07	0.10 ± 0.08	2.16 ± 0.09	0.56 ± 0.06	0.13 ± 0.14	0.13 ± 0.06

Table A.1. Best fit parameters of the cluster scaling relation in Eq. (1).

By using the simplified mean mass-richness relation

$$\langle \ln \lambda | m, z \rangle = \pi(z) + \bar{\mu}_m \ln m, \quad (\text{D.6})$$

where $\bar{\mu}_m$ is linked to the μ_m in Eq. (2) by $\bar{\mu}_m = \mu_m / \ln(10)$, and the results in Evrard et al. (2014) (see their Eq. 3 and 4), we have that

$$\ln \lambda - \langle \ln \lambda | m, z \rangle = \frac{\sigma_{\ln \lambda}^2}{\bar{\mu}_m} \left(\frac{\langle \ln M | \lambda, z \rangle}{\sigma_{\ln M}^2} + \beta_1 \right) - \bar{\mu}_m \ln M. \quad (\text{D.7})$$

Using that $\sigma_{\ln \lambda} = \bar{\mu}_m \sigma_{\ln M}$ (Evrard et al. 2014), we have

$$\ln \lambda - \langle \ln \lambda | m, z \rangle = \frac{\sigma_{\ln \lambda}^2}{\bar{\mu}_m} \beta_1 + \bar{\mu}_m \langle \ln M | \lambda, z \rangle - \bar{\mu}_m \ln M. \quad (\text{D.8})$$

So, by combining Eq. (D.4) and Eq. (D.8), we get

$$\langle \Delta\Sigma | m, \lambda, z \rangle = \langle \Delta\Sigma | m, z \rangle + \frac{\beta_1}{\bar{\mu}_m} \text{Cov}(\Delta\Sigma, \ln \lambda | m, z) \quad (\text{D.9})$$

$$+ \frac{\bar{\mu}_m}{\sigma_{\ln \lambda}^2} \text{Cov}(\Delta\Sigma, \ln \lambda | m, z) (\langle \ln M | \lambda, z \rangle - \ln M). \quad (\text{D.10})$$

From above, we have that the stacked shear decomposes as $\langle \Delta\Sigma \rangle = \langle \Delta\Sigma \rangle_1 + \langle \Delta\Sigma \rangle_2 + \langle \Delta\Sigma \rangle_3$. The first term is given by

$$\langle \Delta\Sigma \rangle_1 = \int_{z_i}^{z_{i+1}} dz \int_{m_{\text{min}}}^{m_{\text{max}}} dm N(m, z) \int_{\lambda_j}^{\lambda_{j+1}} d\lambda P(\lambda | m, z) \langle \Delta\Sigma | m, z \rangle. \quad (\text{D.11})$$

The second term is given by

$$\langle \Delta\Sigma \rangle_2 = \frac{\beta_1}{\bar{\mu}_m} \int_{z_i}^{z_{i+1}} dz \int_{m_{\text{min}}}^{m_{\text{max}}} dm N(m, z) \int_{\lambda_j}^{\lambda_{j+1}} d\lambda P(\lambda | m, z) \text{Cov}(\Delta\Sigma, \ln \lambda | m, z) \quad (\text{D.12})$$

$$\approx \frac{\beta_1}{\bar{\mu}_m} \int_{z_i}^{z_{i+1}} dz \int_{\lambda_j}^{\lambda_{j+1}} d\lambda P(\lambda, z) \text{Cov}(\Delta\Sigma, \ln \lambda | \langle m | \lambda, z \rangle, z) \quad (\text{D.13})$$

$$\approx \frac{\beta_1}{\bar{\mu}_m} \langle \text{Cov}(\Delta\Sigma, \ln \lambda | m, z) \rangle_{ij} \quad (\text{D.14})$$

where the second equation is obtained by considering that $\text{Cov}(\Delta\Sigma, \ln \lambda | m, z)$ evolves linearly with mass m . The term $\langle \Delta\Sigma \rangle_3$ is negligible and not considered in this analysis (see e.g. Wu et al. (2022); Zhang et al. (2024)). Then, from the above equation, we see that a possible shear-richness correlation (e.g. $r \neq 0$, or equivalently $\text{Cov}(\Delta\Sigma, \ln \lambda | m, z) \neq 0$), arising from selection bias in cluster finder algorithms, may lead to a misinterpretation of the stacked cluster profile, as a naive average as given in Eq. (D.11).

Appendix E: Miscentering and contamination with the DC2-redMaPPer galaxy cluster catalog

Appendix E.1: Miscentering

When the identified center of the halo along the line of sight differs from the true center, which happens when deriving it from

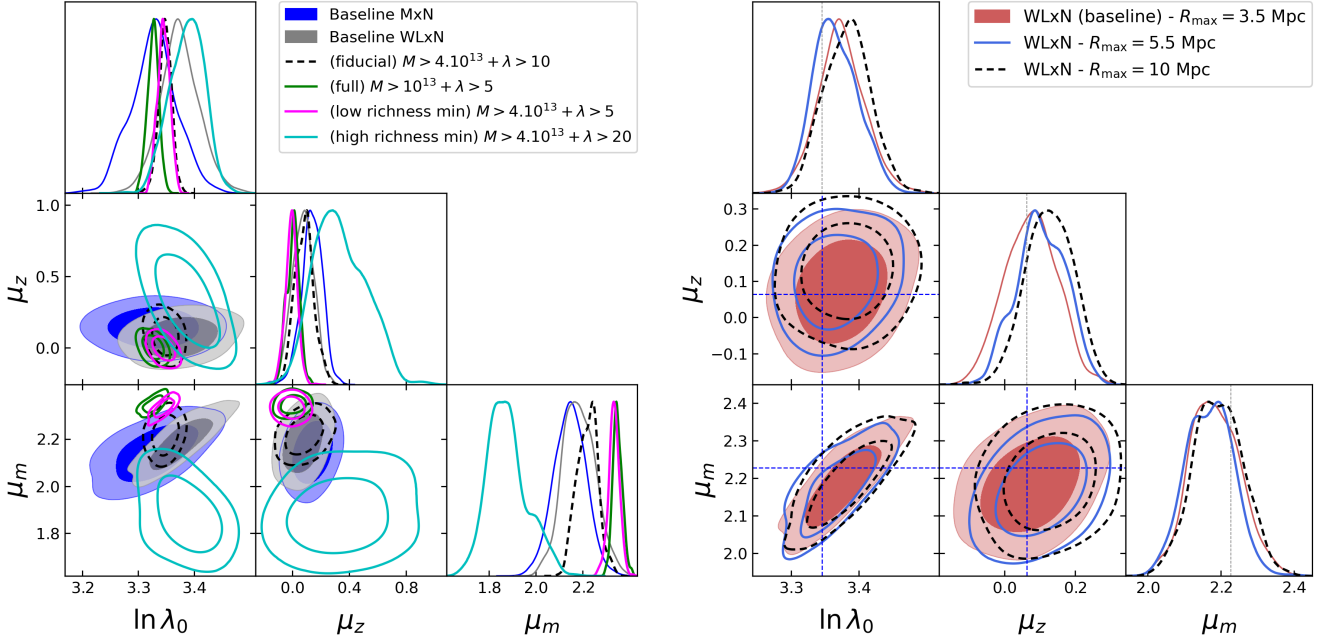


Fig. B.1. Left: Posterior distribution of the mean scaling relation parameters from our count+lensing baselines (filled contours) and the matched redMaPPer-cosmoDC2 cluster-halo match catalog, for different richness and mass cuts. Right: Posterior distribution of the mean scaling relation parameters from the combination of count and lensing profiles, for three different values of R_{\max} , used in the stacked lensing profile fitting range $[1, R_{\max}]$.

the intra-cluster galaxy distribution, the prediction of the lensing profile must account for a mis-centering term. For a single mis-centered cluster with offset radius R_{mis} , its radially averaged projected mass density is given by

$$\Sigma_{\text{mis}}(R, R_{\text{mis}}) = \frac{1}{2\pi} \int_0^{2\pi} d\theta \Sigma \left(\sqrt{R^2 + R_{\text{mis}}^2 + 2RR_{\text{mis}} \cos \theta} \right). \quad (\text{E.1})$$

For a stack of clusters, the above equation can be averaged over the distribution of miscentering $P(R_{\text{mis}})$, such as

$$\Sigma_{\text{mis}}^{\text{stack}}(R) = \frac{1}{2\pi} \int_0^{2\pi} dR_{\text{mis}} P(R_{\text{mis}}) \Sigma_{\text{mis}}(R, R_{\text{mis}}) \quad (\text{E.2})$$

From this equation, we can obtain $\Delta\Sigma_{\text{mis}}$ by injecting in Eq. (18). The total one-halo term depends on the fraction f_{mis} of miscentered clusters, such as (see e.g. Giocoli et al. (2021))

$$\Delta\Sigma_{\text{1h}}(R) = f_{\text{mis}} \Delta\Sigma_{\text{1h,mis}}(R) + (1 - f_{\text{mis}}) \Delta\Sigma_{\text{1h,cen}}(R). \quad (\text{E.3})$$

where $\Delta\Sigma_{\text{1h,cen}}(R)$ denotes the lensing profile of a perfectly centered stack of clusters. To test the impact of miscentering of redMaPPer clusters on the modeling of the stacked excess surface density profiles, we use the matched catalog between redMaPPer clusters and cosmoDC2 dark matter halos obtained in Section 4.4. In each cluster-halo pair, we consider the halo-member galaxy flagged as `is_central==True` in the cosmoDC2 extra-galactic catalog to be the reference *true* center, from which we compute the corresponding projected offset radius R_{mis} of the matched redMaPPer cluster. We found that the fraction of perfectly centered clusters (for which $R_{\text{mis}} = 0$) is 85%, then $f_{\text{mis}} = 0.15$. For pairs with $R_{\text{mis}} \neq 0$, the distribution of offsets between cosmoDC2 halo and redMaPPer cluster centers is well described by a Gamma distribution (McClintock et al. 2019) given by

$$P(R_{\text{mis}}) = \frac{R_{\text{mis}}}{\sigma_{\text{mis}}^2} \exp\left\{-\frac{R_{\text{mis}}}{\sigma_{\text{mis}}}\right\} \quad (\text{E.4})$$

with $\sigma_{\text{mis}} = 0.12$ Mpc. We use the `cluster_toolkit` package³⁰ to compute the miscentered profile evoked in Section 2 over a wide range of mass and redshift, and we found that the bias compared to a perfectly centered profile is at most 1% at $R = 1$ Mpc, and 0.25% at $R = 2$ Mpc. For simplicity, since the computation of the miscentering term is computationally demanding, we will neglect this contribution and consider a 1% systematic bias in our analysis originating from miscentering.

Appendix E.2: Contamination by cluster member galaxies

The observed contaminated lensing profile accounting for this dilution is given by

$$\Delta\Sigma_{ij}^{\text{cont}}(R) = [1 - f_{\text{cl}}(R)] \Delta\Sigma_{ij}(R) \quad (\text{E.5})$$

where $\Delta\Sigma_{ij}(R)$ is given in Eq. (24), $f_{\text{cl}}(R)$ is the fraction of "source-selected" member galaxies at a distance R from the cluster center, and is a decreasing function of R . At fixed R , the fraction f_{cl} increases with mass, since massive clusters have more member galaxies, and thus are more subject to this effect (Varga et al. 2019).

For each redMaPPer cluster, we consider the corresponding matched dark matter halo in the matched catalog presented in Section 4. We applied the photo- z source selection and then identified the remaining halo "member galaxies", as labeled in the simulation (that are randomly drawn at the HOD level in the DC2 workflow to populate halos). This procedure enables us to recover $f_{\text{cl}}(R)$ for a variety of masses and redshift, and we found that the correcting factor $[1 - f_{\text{cl}}(R = 1 \text{ Mpc})] \sim 1$ after combining the two cuts, and for both BPZ and FlexZBoost algorithms. We found that our source selection enables us to discriminate efficiently between true sources and member galaxies (the effect is about less than 0.1%).

³⁰ https://github.com/tmclintock/cluster_toolkit